1

Microlocal Analysis in Tomography

Venkateswaran P. Krishnan[1] and Eric Todd Quinto[2]

[1] Tata Institute for Fundamental Research, Centre for Applicable Mathematics
Bangalore, India
vkrishnan@math.tifrbng.res.in
[2] Tufts University
todd.quinto@tufts.edu

1.1 Introduction

In this chapter, we introduce a range of tomography problems, including X-ray imaging, limited data problems, electron microscopy and radar imaging. We are interested in the recovery of the singular features of the medium or object rather than exact inversion formulas. Toward this end, we show how microlocal analysis helps researchers understand the strengths and limitations inherent in the reconstruction of these and several other tomography problems. Microlocal analysis aids researchers in understanding those singular features that can be stably recovered, which could be very important when only limited or partial data is available. Furthermore, it helps explain the presence of artifacts present in certain image reconstruction methods and in some cases might help distinguish the true singularities from the false ones. We emphasize these issues in this chapter.

In Section 1.2, we will introduce tomography problems including X-ray tomography, electron microscope tomography, and radar imaging. We will present reconstructions for each problem and examine how well they image the original objects with the goal of finding strengths and limitations for each method. In Section 1.3, we introduce some basic properties of some tomographic transforms and then introduce microlocal analysis in Section 1.4. Finally, we give several applications in tomography and radar imaging in Section 1.5 emphasizing the microlocal properties of these transforms. This powerful tool allows us to understand the strengths and limitations that are really intrinsic to the data, as is shown in Section 1.5.

1.2 Motivation

In this section, we provide an introduction to several modalities in tomography, including X-ray tomography, limited data tomography, and electron

microscope tomography. For each type of data, we first provide some history and then examine strengths and weaknesses of reconstructions using such data. The goal of this section is to observe, for each problem, object features that are well reconstructed and features that are not. We provide these reconstructions to motivate the study of microlocal analysis, which we will use in Section 1.5 to explain these reconstructions.

1.2.1 X-ray tomography (CT) and limited data problems

In the 1970's, X-ray tomography revolutionized diagnostic medicine. For the first time, doctors were able to get clear and accurate pictures of the inside of the body without doing exploratory surgery. One part of this story began in the early 1960s. At that time, Allan Cormack consulted as a medical physicist at the Groote Schuur hospital in Cape Town, South Africa, and he checked whether X-ray machines were calibrated properly. He felt that there should be more information in the X-ray data than just what is obtained from single pictures, which project all organs onto the same plane, and he believed that X-rays could be used to image the cross-sectional internal structure of objects. He posited that, if one takes X-ray images from multiple directions, one should be able to piece together the internal structure of the body. He then developed two algorithms [10, 11] for the problem. To give a proof of concept, he built a prototype scanner that showed his second algorithm was effective. Along with Godfrey Hounsfield of EMI in England, he received the 1979 Nobel Prize in Medicine. You can read more about him in the excellent biography [94].

X-ray CT is now used routinely in medicine and in industrial nondestructive testing, and it allows doctors to image the internal structure of the body without exploratory surgery. Here is how we turn the physics of X-ray CT into mathematics. Let ℓ be a line along which X-rays travel, and for $x \in \ell$ let $I(x)$ be the intensity (number of photons) at the point x. Let $f(x)$ be the attenuation coefficient of the body at x. For monochromatic light, f is proportional to the density at x and by using a scale factor they become the same. Beer's Law [65] states that the decrease in intensity at x is proportional the intensity, $I(x)$, and the proportionality constant is $-f(x)$:

$$\frac{dI}{dx} = -f(x)I(x). \tag{1.1}$$

This makes sense heuristically because the more dense the material at x, the more the beam is attenuated and the greater the decrease of I at x. Equation (1.1) is a simple differential equation for I that can be solved using separation of variables. If I_0 is the intensity at the X-ray emitter—the point $x_0 \in \ell$—and I_1 is the intensity at the detector, $x_1 \in \ell$, then we can integrate (1.1) to find

$$\ln\left(\frac{I_0}{I_1}\right) = \int_{x_0}^{x_1} f(x)\,\mathrm{d}x = \int_{x\in\ell} f(x)\,\mathrm{d}x\,.$$

So, we define

$$\mathcal{R}_L(f)(\ell) = \int_{x\in\ell} f(x)\,\mathrm{d}x$$

where in this case, $\mathrm{d}x$ is the arc length measure on ℓ. The transform $\mathcal{R}_L$ was studied by the Austrian mathematician Johann Radon [81] in the early twentieth century because it was intriguing pure mathematics. This transform is called the *Radon line transform* (or X-ray transform).

To proceed mathematically, we now establish more notation. Let $\omega \in S^1$ and let $p \in \mathbb{R}$. Then, the line

$$\ell(\omega, p) = \{x \in \mathbb{R}^2 \,:\, x \cdot \omega = p\} \tag{1.2}$$

is perpendicular to ω and contains $p\omega$. Sometimes it will be useful to let ω be a function of polar angle $\varphi \in \mathbb{R}$,

$$\omega(\varphi) = (\cos(\varphi), \sin(\varphi)) \ .$$

In this parameterization

$$\mathcal{R}_L f(\omega, p) = \int_{x\in\ell(\omega,p)} f(x)\,\mathrm{d}x = \int_{t\in\mathbb{R}} f(p\omega + t\omega^\perp)\,\mathrm{d}t \tag{1.3}$$

where $\omega^\perp$ is the unit vector $\pi/2$ radians counterclockwise from ω. This integral is defined for $f \in C_c(\mathbb{R}^2)$ and in fact $\mathcal{R}_L$ is continuous on many spaces (see Section 1.3.3). We will prove the basic properties of this transform in Section 1.3.

First, we consider the forward problem and a simple case that will show in a naive sense how the X-ray transform detects object boundaries.

Example 1. Let f be the characteristic function of the unit disk in $\mathbb{R}^2$. Then, using the Pythagorean Theorem,

$$\mathcal{R}_L f(\omega, p) = \begin{cases} 2\sqrt{1-p^2} & |p| \leqslant 1 \\ 0 & |p| > 1 \end{cases} . \tag{1.4}$$

The function $\mathcal{R}_L f(\omega, p)$ in (1.4) is smooth except at $p = \pm 1$, that is, except for lines $\ell(\omega, \pm 1)$ as can be seen from Figure 1.1. The data are not smooth at those lines and these lines are tangent to the boundary of the disk. This suggests that lines tangent to boundaries give special information about the specimen. In Section 1.4, we will discover what is mathematically special about those lines and we will relate this back to limited data tomography in Section 1.5.

For complete data, that is data over all lines through the object, good reconstruction methods such as Filtered backprojection (Theorem 9) are effective to reconstruct from X-ray CT data.

However one cannot obtain complete data in many important tomography problems. These are called *limited data tomography problems*, and we will now describe several important ones. Our goal at this point is to observe how the

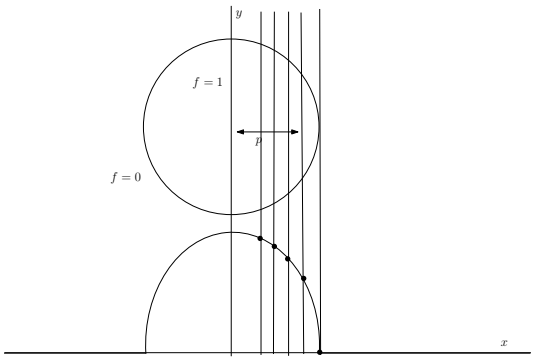

Fig. 1.1. This graph shows the calculation of the Radon transform in (1.4). The unit disk is above the graph. For $|p| \leqslant 1$, one can see that the length of the intersection of $\ell(\omega, p)$ and the disk is $2\sqrt{1-p^2}$.

reconstructions look compared to the original objects. We will use this to help understand these problems.

Here are some guidelines as you read this section. For each problem and reconstruction, conjecture what is special about the object boundaries that are well reconstructed in relation to the limited data set used. Also, think about what is special about those boundaries that are not well reconstructed.

Exterior X-ray CT Data

Exterior CT data are data for lines that are outside an excluded region. Typically, that region is a circle of radius $r > 0$, so lines $\ell(\omega, p)$ for $|p| \geqslant r$ are in the data set. Theorem 5 in the next section shows that compactly supported functions can be uniquely reconstructed outside the excluded region from exterior data.

The exterior problem came about in the early days of tomography for CT scans around the beating heart. In those days, a single scan of a planar cross section could take several minutes, and movement of the heart would create artifacts in the scan. If an excluded region were chosen to contain the heart and be large enough so the outside of that region would not move, then data exterior to that region would be usable. However, scanners soon began to use fan beam data (see Section 1.3.6) and data could be acquired much more quickly. If the data acquisition is timed (gated) then data are acquired while the heart is in the same position over several heartbeats. Because more data can be taken more quickly with fan beam data, the heart can now be imaged using newer scanners, and movement of the heart is not as large a problem.

Exterior data are still important for imaging large objects such as rocket shells. Even with an industrial CT scanner, the X-rays will not penetrate the

thick center of the rocket [85]. However, they can penetrate the outer rocket shell, and this gives exterior data.

One can recover functions of compact support from exterior data, at least outside the excluded region (see Theorem 5). Effective inversion methods were developed for exterior data by researchers including Bates and Lewitt [3], Natterer [64], Quinto [74, 76] and a stability analysis using a singular value decompositions was done in [57].

We now present a reconstruction from exterior data: integrals are given over lines that do not meet the black central disk. The reconstruction method

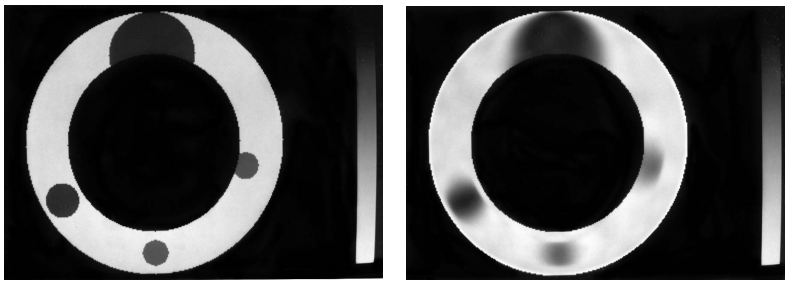

Fig. 1.2. Phantom (left) and exterior reconstruction [74, ©IOP Publishing. Reproduced by permission of IOP Publishing. All rights reserved] from simulated data. The outer diameter of the annulus is 1.5 times the inner diameter.

uses a singular value decomposition for the exterior Radon transform that includes a null space; it recovers the component of the object in the orthogonal complement of the null space and does an interpolation to recover the null space component [74].

Note how some boundaries of the small circles are clearly reconstructed and others are not. In this case, how can you describe the boundaries that are well reconstructed in relation to the data set? Another question is whether the fuzzy boundaries are fuzzy because the algorithm is bad or could there be an additional explanation?

Allan Cormack's first algorithm [10] solved the exterior problem, but the algorithm did not work numerically. The integrals in his algorithm were difficult to evaluate numerically with any accuracy because the integrand grew too rapidly. Other mathematicians tried to improve this method but it was difficult. Because of this problem, Cormack developed a second method that uses full data and that gave good reconstructions [11].

It would be useful to know if limitations of Quinto's and Cormack's algorithms are problems with their algorithms or reflect something intrinsic to this limited data problem.

Limited Angle Data

Limited angle tomography is a classical problem from the early days of tomography [3, 59, 60]. In this case, data are given over all lines in a limited range of directions, or data for $\{(\omega(\varphi), p) : \varphi \in (a, b), p \in \mathbb{R}\}$ where $b - a < \pi$. It is used in certain luggage scanners in which the X-ray source is on one side of the luggage and the detectors are on the other and they move in opposite directions. One can uniquely recover compactly supported functions from limited angle data but this is not true in general (see Theorem 3). Limited angle data are used in important current problems including dental X-ray scanning [47], tomosynthesis (a tomographic technique to image breasts using transmitter and receiver that move on opposite sites of the breast) [70]. Other algorithms were developed for this problem such as [50, 12, 47, 24].

The reconstruction in Fig. 1.3 is from limited angle data. Data are taken over all lines $\ell(\omega(\varphi), p)$ for $p \in \mathbb{R}$ and $\varphi \in [-\pi/4, \pi/4]$. The algorithm used in

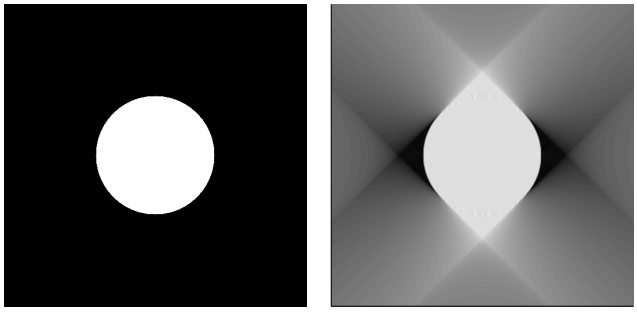

Fig. 1.3. Original image (left) and a truncated Filtered Backprojection (FBP) reconstruction algorithm (right) using data in the angular range, $\varphi \in [-\pi/4, \pi/4]$. Note the streak artifacts and the missing boundaries in the limited angle reconstructions [24,].

this reconstruction is a truncated Filtered Backprojection (FBP) algorithm which is given in (1.26). Some boundaries in this reconstruction are well-reconstructed and others are not. How do these boundaries relate to lines in the data set? There are streak artifacts along certain lines. How do these streaks relate to the data set?

Region of Interest (ROI) Data

One chooses a subregion of the object, also called a *region of interest (ROI)*, to reconstruct. ROI data consist of all lines that meet this region, and the ROI problem is to reconstruct the structure of the ROI from these data. This

is also called interior data (and the interior problem). ROI CT is important in the CT of small parts of objects, so called micro-CT [16, p. 460]. Other algorithms in ROI CT include [98] (if one knows the value of a function in part of the interior), [99] (if the density is piecewise constant in the ROI) and others including [49]. A singular value decomposition was developed for this problem in [62].

ROI CT is useful for medical CT and industrial nondestructive evaluation in which one is interested only in a small region of interest in an object, not the entire object. An advantage for medical applications is that ROI data gives less radiation than with complete data.

Lambda tomography [15], [16] is one important algorithm for ROI-CT which will be described in section 1.3.4, and our ROI reconstruction uses this algorithm. In this case, note that all the singularities of this simple object are

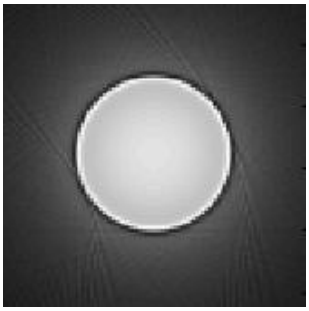

Fig. 1.4. ROI reconstruction from simulated data for the characteristic function of a circle using the operator $\mathcal{L}_{x,\mu}$ given in (1.23) [4, ©Tufts University].

visible, even though the data are severely limited–they include only lines near the disk. On the other hand, the ROI transform is not injective (see Theorem 6), so why do the reconstructions look so good?

Limited Angle Region of Interest Tomography

In this modality data are given over lines in a limited angular range and that are restricted to pass through a given ROI. It comes up in single axis tilt electron microscopy (ET) (see Öktem's chapter in this book [69]). However, in general, ET is better understood as a three-dimensional problem and we will discuss it that way in the next paragraph.

1.2.2 Electron Microscope Tomography (ET) over arbitrary curves

Now we consider a full three dimensional problem, electron microscope tomography (ET), and we follow the notation in Öktem's chapter in this book [69],

which has detailed information about the physics, biology, model and mathematics of ET. We show a reconstruction from a simple 3D phantom, the union of the following disks: with center $(0, 0, 0)$ radius $1/2$, center $(0, 0, 1)$ radius $1/2$ center $(1, -1, 1)$ radius $1/4$ center $(-1, 1, -1/2)$ radius $1/4$. The disks above the $x - y$-plane have density two and the others have density one.

We consider conical tilt ET data, which is described in Öktem's chapter in this book [69]. In our case, line integrals are given over all lines in space with angle $\alpha = \pi/4$ with the $z-$axis. We will consider reconstructions from two algorithms that are described in Section 1.2.2. The operators are $\mathcal{L}_\Delta$ (given in equation (1.28)) and $\mathcal{L}_S$ (given in equation (1.29)).

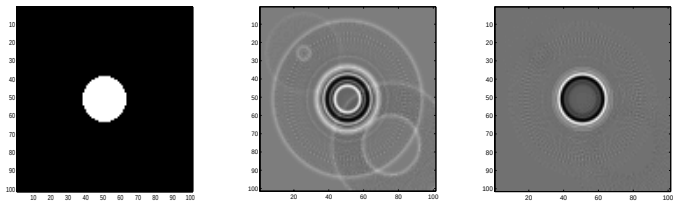

Fig. 1.5. Cross-section with the $x-y$ plane of the phantom described in this section (left), $\mathcal{L}_\Delta$ reconstruction (center, see eq. (1.28)) and $\mathcal{L}_S$ reconstruction (right, see eq. (1.29)). The center of the cross-section is the origin and the range in x and y is from -2 to 2 [79, Reproduced with kind permission from Springer Science+Business Media: ©Springer Verlag].

Artifacts are added in the $\mathcal{L}_\Delta$ reconstruction in Figure 1.5 and in Figure 1.6 which shows the plane containing the centers of the disks and the $z-$axis (axis of rotation of the scanner). These figures are remarkable because the $\mathcal{L}_\Delta$

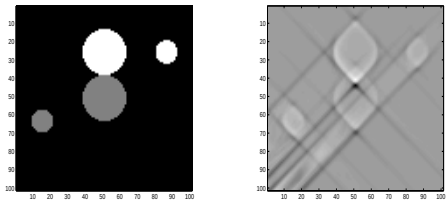

Fig. 1.6. Cross-section of phantom in the plane $x = -y$ (left) and $\mathcal{L}_\Delta$ reconstruction in that plane(right). The $x - y$-plane cuts the picture in half with a horizontal line. [79, Reproduced with kind permission from Springer Science+Business Media: ©Springer Verlag]

reconstruction has so many added artifacts compared to the $\mathcal{L}_S$ reconstruction

although these operators are not very different (see Section 1.3.7. Why are the reconstructions so different?

Reconstructions of real specimens from single axis tilt data show some of the same strengths and limitations (see, e.g., [77, 80] and Öktem's chapter in this book [69]). However, the added artifacts have different properties, and since the data are so noisy, other factors affect reconstructions.

1.2.3 Synthetic aperture radar Imaging

In synthetic aperture radar (SAR) imaging, a region of interest on the surface of the earth is illuminated by electromagnetic waves from an airborne platform such as a plane or satellite. For more detailed information on SAR imaging, including several open problems in SAR imaging, we refer the reader to [7, 8] and to the chapter in this handbook by Cheney and Borden [9]. The backscattered waves are picked up at a receiver or receivers and the goal is to reconstruct an image of the region based on such measurements. In monostatic SAR, the transmitter and receiver are located on the same platform. In bistatic SAR, the transmitter and receiver are on independently moving trajectories. While monostatic SAR imaging is the one that is widely used, bistatic SAR imaging offers several advantages in certain imaging situations. The receivers in comparison to transmitters are not active sources of electromagnetic radiation and hence are more difficult to detect if flown in an unsafe environment. Since the transmitter and receiver are at different points in space, bistatic SAR systems are more resistant to electronic countermeasures such as target shaping to reduce scattering in the direction of incident waves [46]. The reconstruction of the image based on the measurement of the backscattered waves is in general a hard problem. However, ignoring contributions of multiply backscattered waves linearizes the relation between the image to be recovered and the backscattered waves and is easier to analyze. Due to this reason, a linearizing approximation called the Born approximation that ignores contribution from multiply scattered waves is widely used in SAR image reconstruction.

The linearized model in SAR imaging

Let $\gamma_T(s)$ and $\gamma_R(s)$ for $s \in (s_0, s_1)$ be the trajectories of the transmitter and receiver respectively. The propagation of electromagnetic waves can be described by the scalar wave equation:

$$\left(\Delta - \frac{1}{c^2}\partial_t^2\right) E(x,t) = -P(t)\delta(x - \gamma_T(s)), \tag{1.5}$$

where c is the speed of electromagnetic waves in the medium, $E(x,t)$ is each component of the electric field and $P(t)$ is the transmit waveform sent to the

transmitter antenna. The wave speed c is spatially varying due to inhomogeneities present in the medium and we assume that it is a perturbation of the constant background speed of propagation c_0 of the form

$$\frac{1}{c^2(x)} = \frac{1}{c_0^2} + \widetilde{V}(x).$$

We assume that $\widetilde{V}(x)$ only varies over a 2-dimensional surface; the surface of the earth. Therefore, we represent $\widetilde{V}$ as a function of the form

$$\widetilde{V}(x) = V(x)\delta_0(x_3)$$

where we assume that the earth's surface is represented by the $x = (x_1, x_2)$ plane. The background Green's function g is the solution of the following equation:

$$\left(\Delta - \frac{1}{c_0^2}\partial_t^2\right) g(x,t) = -\delta_0(x)\delta_0(t).$$

This is given by

$$g(x,t) = \frac{\delta(t - \|x\|/c_0)}{4\pi \|x\|}. \tag{1.6}$$

Now the incident field E^{in} due to the source $s(x,t) = P(t)\delta(x - \gamma_T(s))$ is

$$\begin{aligned} E^{\text{in}}(x,t) &= \int g(x-y, t-\tau)s(y,\tau)\mathrm{d}y\mathrm{d}\tau \\ &= \frac{P(t - \|x - \gamma_T(s)\|/c_0)}{4\pi \|x - \gamma_T(s)\|}. \end{aligned}$$

Let E denote the total field of the medium, $E = E^{\text{in}} + E^{\text{sc}}$, where E^{sc} is the scattered field. This can be written using the Lippman-Schwinger equation:

$$E^{\text{sc}}(z,t) = \int g(z-x, t-\tau)\partial_t^2 E(x,\tau)V(x)\mathrm{d}x\mathrm{d}\tau. \tag{1.7}$$

We linearize this equation by replacing the total field E on the right hand side of the above equation by E^{in}. This is known as the Born approximation. The linearized scattered wave-field $E^{\text{sc}}_{\text{lin}}(\gamma_R(s), t)$ at the receiver location $\gamma_R(s)$ is then

$$E^{\text{sc}}_{\text{lin}}(\gamma_R(s), t) = \int g(x - \gamma_R(s), t-\tau)\partial_t^2 E^{\text{in}}(x,\tau)V(x)\mathrm{d}x\mathrm{d}\tau$$

Substituting the expression for E^{in} into this equation and integrating, we obtain the following expression for the linearized scattered wave-field:

$$E^{\text{sc}}_{\text{lin}}(\gamma_R(s), t) = \int e^{-\mathrm{i}\omega(t - \frac{1}{c_0}R(s,x))} A(s,x,\omega)V(x)\mathrm{d}x\mathrm{d}\omega, \tag{1.8}$$

where

$$R(s,x) = \|\gamma_T(s) - x\| + \|x - \gamma_R(s)\|$$

and

$$A(s,x,\omega) = \omega^2 p(\omega)((4\pi)^2 \|\gamma_T(s) - x\| \|\gamma_R(s) - x\|)^{-1}, \tag{1.9}$$

where p is the Fourier transform of P. The function A includes terms that take into account the transmitted waveform and geometric spreading factors. The inverse of the norms appear in A due to the background Green's function, (1.6).

The following image reconstruction of a disc centered on the positive y-axis from integrals of it over ellipses with foci moving along the x-axis offset by a constant distance (which is simplified model of (1.8)) highlights some of the features in SAR image reconstruction. Some part of the boundary is not stably reconstructed and an artifact of the true image appears as a reflection about the x-axis along with streak artifacts. Looking at the reconstructed image, one sees that, at least visually, the created artifact is as strong as the true image. Microlocal analysis of the operators appearing in SAR imaging will make precise and justify all these observations. We will address them in Section 1.5.4.

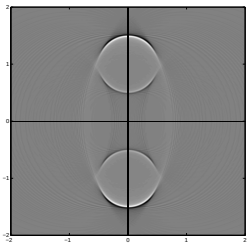

Fig. 1.7. Reconstruction of a disk centered on the positive $y-$axis from integrals over ellipses (with constant distance between the foci) centered on the x-axis and with foci in [-3,3]. Notice that some boundaries of the disk are missing, and there is a copy of the disk below the axis. This was originally from the Tufts University Senior Honors Thesis of Howard Levinson and published in [54, Reproduced with kind permission from Springer Science+Business Media: © Springer Verlag].

1.2.4 General Observations

In each reconstruction for two dimensional X-ray CT in this section, some object boundaries are visible and others are not. In fact, if one looks more carefully at the reconstructions, one can notice that, in each case, the only feature boundaries that are clear defined are those tangent to lines in the data set for the problem. Example 1 illustrates this in a naive way: one sees singularities in the Radon data exactly when the lines of integration are tangent

to the boundary of the object. The goal of this chapter is to make the idea mathematically rigorous.

The conical tilt ET reconstructions in Section 1.2.2 have artifacts if one uses a certain algorithm but not when one uses another similar one. The reconstruction related to Radar in Figure 1.7 has an artifact that is a reflected image of the disk.

In Section 1.4, we will introduce deep mathematical ideas from microlocal analysis to classify singularities and understand what operators do to them. In Section 1.5 we will use these microlocal ideas to explain the visible and invisible singularities for limited data X-ray CT as well as the added singularities in ET and Radar.

1.3 Properties of Tomographic Transforms

In this section, after introducing some functional analysis, we present the basic properties of transforms in X-ray tomography and electron microscope tomography. We will study the microlocal properties of Radar in Section 1.5.4.

1.3.1 Function Spaces

We start with some basic notation. The open disk in $\mathbb{R}^2$ centered at the origin and of radius $r > 0$ will be denoted $D(r)$.

The set $C^\infty(\mathbb{R}^n)$, consists of all smooth functions on $\mathbb{R}^n$, that is functions that are continuous along with their derivatives of all orders, and $\mathcal{D}(\mathbb{R}^n)$is the set of smooth functions of compact support. Its dual space–the set of all continuous linear functionals on $\mathcal{D}(\mathbb{R}^n)$ (given the weak-* topology)–is denoted $\mathcal{D}'(\mathbb{R}^n)$ and is called the *set of distributions*. If u is a locally integrable function then u is a distribution with the standard definition

$$\langle u, f\rangle = u(f) = \int_{\mathbb{R}^n} u(x)f(x)\,\mathrm{d}x$$

for $f \in \mathcal{D}(\mathbb{R}^n)$ since $u(x)f(x)$ is an integrable function of compact support.

The *Schwartz Space* of rapidly decreasing functions is the set $\mathcal{S}(\mathbb{R}^n)$ of all smooth functions that decrease (along with all their derivatives) faster than any power of $1/\|x\|$ at infinity. Its dual space, $\mathcal{S}'(\mathbb{R}^n)$ is the set of all continuous linear functionals on $\mathcal{S}(\mathbb{R}^n)$ with the weak-* topology (convergence is pointwise: $u_k \to u$ in $\mathcal{S}'(\mathbb{R}^n)$ if, for each $f \in \mathcal{S}(\mathbb{R}^n)$, $u_k(f) \to u(f)$). They are called *tempered distributions*. Any function that is measurable and polynomially increasing is in $\mathcal{S}'(\mathbb{R}^n)$ since its product with any Schwartz function is integrable.

A distribution u has support the closed set K if for all functions $f \in \mathcal{D}(\mathbb{R}^n)$ with support disjoint from K, $u(f) = 0$.

Example 2. The *Dirac Delta function at zero* is an important distribution that is not a function. It is defined $\langle \delta_0, f \rangle = \delta_0(f) = f(0)$. Note that if f is supported away from the origin then $\delta_0(f) = 0$ since $f(0) = 0$. Therefore, the Dirac Delta function has support $\{0\}$.

We let $\mathcal{E}'(\mathbb{R}^n)$ be the set of distributions that have compact support in $\mathbb{R}^n$. If Ω is an open set in $\mathbb{R}^n$, then $\mathcal{E}'(\Omega)$ is the set of distributions with compact support contained in Ω. For example, on the real line, $\delta \in \mathcal{E}'((-1,1))$.

If $f \in L^1(\mathbb{R}^n)$ then the Fourier transform and its inverse are

$$\begin{aligned} \mathcal{F}f(\xi) = \widehat{f}(\xi) &= \frac{1}{(2\pi)^{n/2}} \int_{x\in\mathbb{R}^n} e^{-ix\cdot\xi} f(x)\,\mathrm{d}x \\ \mathcal{F}^{-1}f(x) = \check{f}(x) &= \frac{1}{(2\pi)^{n/2}} \int_{\xi\in\mathbb{R}^n} e^{ix\cdot\xi} f(\xi)\,\mathrm{d}\xi\,. \end{aligned} \tag{1.10}$$

The Fourier transform is linear and continuous from $L^1(\mathbb{R}^n)$ to the space of continuous functions that converge to zero at ∞. Furthermore, $\mathcal{F}$ is an isomorphism on $L^2(\mathbb{R}^n)$ and an isomorphism on $\mathcal{S}(\mathbb{R}^n)$ and, therefore, on $\mathcal{S}'(\mathbb{R}^n)$. More information about these topics can be found in [83], for example.

1.3.2 Basic properties of the Radon Line Transform

In this section we derive fundamental properties of the Radon line transform $\mathcal{R}_L$, and this will allow us to make a connection between the transforms and the microlocal analysis in Section 1.4.

Theorem 1 (General Projection Slice Theorem). *Let $f \in L^1(\mathbb{R}^2)$. Now let $h \in L^\infty(\mathbb{R})$ and $\omega \in S^1$. Then,*

$$\int_{x\in\mathbb{R}^2} f(x)h(x\cdot\omega)\,\mathrm{d}x = \int_{p=-\infty}^{\infty} \mathcal{R}_L f(\omega,p)h(p)\,\mathrm{d}p. \tag{1.11}$$

Proof. Let $\omega \in S^1$. First, note that the function $x \mapsto f(x)h(x\cdot\omega)$ is in $L^1(\mathbb{R}^2)$ since h is bounded and measurable. For the same reason, the function

$$(p,t) \mapsto f(p\omega + t\omega^\perp)h(p)$$

is in $L^1(\mathbb{R}^2)$. We have that

$$\begin{aligned} \int_{x\in\mathbb{R}^2} f(x)h(x\cdot\omega)\,\mathrm{d}x &= \int_{p=-\infty}^{\infty}\int_{t=-\infty}^{\infty} f(p\omega + t\omega^\perp)h\,(p)\;\mathrm{d}t\,\mathrm{d}p \qquad (1.12)\\ &= \int_{p=-\infty}^{\infty} \mathcal{R}_L f(\omega,p)h(p)\,\mathrm{d}p \qquad (1.13) \end{aligned}$$

where (1.12) holds by rotation invariance of the Lebesgue integral and then Fubini's theorem and since $p = \omega\cdot(p\omega + t\omega^\perp)$. The equality (1.13) holds by the definition of $\mathcal{R}_L$. □

The *partial Fourier transform* is defined for $g \in L^1(S^1 \times \mathbb{R})$ as

$$\mathcal{F}_p g(\omega, \tau) = \frac{1}{\sqrt{2\pi}} \int_{p \in \mathbb{R}} e^{-ip\tau} g(\omega, \tau) \, \mathrm{d}\tau \,. \tag{1.14}$$

Because the Fourier transform is an isomorphism on $\mathcal{S}(\mathbb{R})$, this transform and its inverse are defined and continuous on $\mathcal{S}'(S^1 \times \mathbb{R})$.

The *Fourier Slice Theorem* is an important corollary of Theorem 1.

Theorem 2 (Fourier Slice Theorem). *Let $f \in L^1(\mathbb{R}^2)$. Then for $(\omega, \tau) \in S^1 \times \mathbb{R}$,*

$$\mathcal{F}f(\tau\omega) = \frac{1}{\sqrt{2\pi}} \mathcal{F}_p \mathcal{R}f(\omega, \tau) \,.$$

To prove this theorem, we apply the General Projection Slice Theorem 1 to the function $h(p) = e^{-ip\tau}$.

The Fourier Slice Theorem provides a quick proof that $\mathcal{R}_L$ is invertible on domain $L^1(\mathbb{R}^2)$ since $\mathcal{F}_p$ is invertible on domain $L^1(S^1 \times \mathbb{R})$. Zalcman constructed a nonzero function that is integrable on every line in the plane and whose line transform is identically zero [101]. Of course, his function is not in $L^1(\mathbb{R}^2)$.

This theorem also provides a quick proof of invertibility for the limited angle problem.

Theorem 3 (Limited Angle Theorem). *Let $f \in \mathcal{E}'(\mathbb{R}^2)$ and let $a < b$ and $b - a < \pi$. If $\mathcal{R}_L f(\omega(\varphi), p) = 0$ for $\varphi \in (a, b)$ and all p, then $f = 0$.*

However, there are nonzero functions $f \in \mathcal{S}(\mathbb{R}^2)$ with $\mathcal{R}_L f(\omega(\varphi), p) = 0$ for $\varphi \in (a, b)$ and all p.

Proof. Let $f \in \mathcal{E}'(\mathbb{R}^2)$ and assume $\mathcal{R}_L f(\omega(\varphi), p) = 0$ for $\varphi \in (a, b)$ and all p. By the Fourier Slice Theorem, which is true for $\mathcal{E}'(\mathbb{R}^2)$ [42],

$$\mathcal{F}f(\tau\omega(\varphi)) = \frac{1}{\sqrt{2\pi}} \mathcal{F}_p \mathcal{R}_L f(\omega(\varphi), \tau) = 0 \quad \text{for } \varphi \in (a, b),\ \tau \in \mathbb{R} \tag{1.15}$$

and this expression is zero because $\mathcal{R}_L f(\omega(\varphi), \tau) = 0$ for such (φ, τ). This shows that $\mathcal{F}f$ is zero on the open cone

$$V = \{\tau\omega(\varphi) \,:\, \tau \neq 0, \varphi \in (a, b)\}.$$

Since f has compact support, $\mathcal{F}f$ is real analytic, and so $\mathcal{F}f$ must be zero everywhere since it is zero on the open set V. This shows $f = 0$.

To prove the second part of the theorem, let $\tilde{f}$ be any nonzero Schwartz function supported in the cone V and let $f = \mathcal{F}^{-1}\left(\tilde{f}\right)$. Since $\tilde{f}$ is nonzero and in $\mathcal{S}(\mathbb{R}^2)$, so is f. Using (1.15) but starting with $\mathcal{F}f = 0$ in V, we see $\mathcal{R}_L f$ is zero in the limited angular range. □

Another application of these theorems is the classical range theorem for this transform. We let $\mathcal{S}(S^1 \times \mathbb{R})$ be the set of smooth functions on $S^1 \times \mathbb{R}$ that decrease (along with all their derivatives) faster than any power of $1/|p|$ at infinity uniformly in ω.

Theorem 4 (Range Theorem [38, 26]). *Let $g \in \mathcal{S}(S^1 \times \mathbb{R})$. Then g is in the range of $\mathcal{R}_L$ on domain $\mathcal{S}(\mathbb{R}^2)$ if and only if*

1. $g(\omega, p) = g(-\omega, -p)$
2. *for each $m \in \{0, 1, 2, \ldots\}$, $\displaystyle\int_{p\in\mathbb{R}} g(\omega, p)p^m \,\mathrm{d}p$ is a polynomial in $\omega \in S^1$ that is homogeneous of degree m.*

Proof (Proof Sketch). The necessary part of the theorem follows by applying the General Projection Slice Theorem to $h(p) = p^m$ for m a nonnegative integer:

$$\int_{p\in\mathbb{R}} \mathcal{R}_L f(\omega, p)p^m \,\mathrm{d}p = \int_{x\in\mathbb{R}^2} f(x)(x \cdot \omega)^m \,\mathrm{d}x$$

and after multiplying out $(x \cdot \omega)^m$ in the coordinates of ω, one sees that the right hand integral is a polynomial in these coordinates of order at most m. The sufficiency part is much more difficult to prove. One uses the Fourier Slice Theorem to construct a function f satisfying $\mathcal{F}f(\tau\omega) = \frac{1}{\sqrt{2\pi}}\mathcal{F}_p g(\omega, \tau)$. Since $\mathcal{F}_p g$ is smooth and rapidly decreasing in p, $\mathcal{F}f$ is smooth away from the origin and rapidly decreasing in x. The subtle part of the proof in [38] is to show $\mathcal{F}f$ is smooth at the origin, and this is done using careful estimates on derivatives using the moment conditions, 2. Once that is known, one can conclude $\mathcal{F}f \in \mathcal{S}(\mathbb{R}^2)$ and so $f \in \mathcal{S}(\mathbb{R}^2)$. □

The support theorem for $\mathcal{R}_L$ is elegant and has motivated a large range of generalizations such as [39, 6, 5, 56, 52, 75].

Theorem 5 (Support Theorem [10, 26, 38]). *Let f be a distribution of compact support (or a function in $\mathcal{S}(\mathbb{R}^2)$) and let $r > 0$. Assume $\mathcal{R}_L f$ is zero for all lines that are disjoint from the disk $D(r)$. Then* $\mathrm{supp}(f) \subset D(r)$.

There are null functions for the exterior transform and they do not decrease rapidly at infinity [71, 73] and simple examples are given in [100, 40].

This theorem implies that the exterior problem has a unique solution; in this case $D(r)$ is the excluded region. The proof is tangential to the main topics of this chapter, so we refer to [10, 26, 38, 40, 89] for proofs.

Counterexamples to the support theorem exist for functions that do not decrease rapidly at ∞, (e.g., [40] or the singular value decompositions in [71, 73]).

A corollary of these theorems shows that exact reconstruction is impossible from ROI data where $D(r)$ is the disk centered at the origin in $\mathbb{R}^2$ and of radius $r > 0$.

Theorem 6. *Consider the ROI problem with region of interest the unit disk $D(1)$. Let $r \in (1, \infty)$. Then there is a function $f \in \mathcal{D}(D(r))$ that is not identically zero in $D(1)$ but for which $\mathcal{R}_L f$ is zero for all lines that intersect $D(1)$.*

Proof (Proof Sketch). Let $h(p)$ be a smooth nonzero nonnegative function supported in $(1, r)$ and let $g(\omega, p) = h(|p|)$. Since g is independent of ω, the moment conditions from the Range Theorem, 2, are trivially satisfied, so that theorem shows that there is a function $f \in \mathcal{S}(\mathbb{R}^2)$ with $\mathcal{R}_L f = g$. By the support theorem, f is supported in the disk $D(r)$. To show f is nonzero in the ROI, $D(1)$, one uses [10, p. 2725, equation (18)]. This is also proven in [65, p. 169, VI.4], and Natterer shows that such null functions do not oscillate much in the ROI. We will show in Section 1.5 that null functions are smooth in the ROI, too. □

1.3.3 Continuity results for the X-ray Transform

In this section we present some basic continuity theorems for $\mathcal{R}_L$.

A simple proof shows that $\mathcal{R}_L$ is continuous from $C_c(D(M))$ to $C_c(S_M)$ where $S_M = S^1 \times [-M, M]$. First, one uses uniform continuity of f to show $\mathcal{R}_L f$ is a continuous function. Then, the proof that $\mathcal{R}_L$ is continuous is based on the estimate

$$|\mathcal{R}_L f(\omega, p)| \leqslant \pi M^2 \|f\|_\infty$$

where $\|f\|_\infty$ is the (essential) supremum norm of f. A stronger theorem has been proven by Helgason.

Theorem 7 ([38]). $\mathcal{R}_L : \mathcal{S}(\mathbb{R}^2) \to \mathcal{S}(S^1 \times \mathbb{R})$ *is continuous.*

The proof of our next theorem follows from the calculations in the proof of the General Projection Slice Theorem.

Theorem 8. $\mathcal{R}_L : L^1(\mathbb{R}^2) \to L^1(S^1 \times \mathbb{R})$ *is continuous.*

Proof. By taking absolute values in (1.11) with $h = 1$ and then integrating with respect to ω, one sees that $\|f\|_{L^1(\mathbb{R}^2)} \geqslant (2\pi) \|\mathcal{R}_L f\|_{L^1(S^1 \times \mathbb{R})}$ and so $\mathcal{R}_L$ is continuous on L^1. □

Continuity results for $\mathcal{R}_L$ in Sobolev spaces were given in [58, 42, 37] for functions of fixed compact support.

1.3.4 Filtered Backprojection (FBP) for the X-ray Transform

To state the most commonly used inversion formula, Filtered Back Projection, we begin by defining the *Dual Line Transform*. For $g \in L^1(S^1 \times \mathbb{R})$ and $x \in \mathbb{R}^2$,

$$\mathcal{R}_L^* g(x) = \int_{\omega \in S^1} g(\omega, x \cdot \omega) \, \mathrm{d}\omega. \tag{1.16}$$

For each $\omega \in S^1$, $x \in \ell(\omega, x \cdot \omega)$, so $\mathcal{R}_L^* g(x)$ is the integral of g over all lines through x. The transform $\mathcal{R}_L^*$ is the formal dual to $\mathcal{R}_L$ in the sense that, for $f \in \mathcal{S}(\mathbb{R}^2)$ and $g \in \mathcal{S}(S^1 \times \mathbb{R})$,

$$\langle \mathcal{R}_L f, g \rangle_{L^2(S^1 \times \mathbb{R})} = \langle f, \mathcal{R}_L^* g \rangle_{L^2(\mathbb{R}^2)} \ .$$

Because $\mathcal{R}_L : \mathcal{S}(\mathbb{R}^2) \to \mathcal{S}(S^1 \times \mathbb{R})$ is continuous, $\mathcal{R}_L^* : \mathcal{S}'(S^1 \times \mathbb{R}) \to \mathcal{S}'(\mathbb{R}^2)$ is weakly continuous.

The Lambda operator is defined on functions $g \in \mathcal{S}(S^1 \times \mathbb{R})$ by

$$\Lambda_p g(\omega, p) = \mathcal{F}_p^{-1} \left(|\tau| \left(\mathcal{F}_p g(\omega, \cdot) \right) \right) . \tag{1.17}$$

Theorem 9 (Filtered Backprojection (FBP) [82, 84, 65]). *Let $f \in \mathcal{S}(\mathbb{R}^2)$. Then,*

$$f = \frac{1}{4\pi} \mathcal{R}_L^* \Lambda_p \mathcal{R}_L f \tag{1.18}$$

This formula is valid for $f \in \mathcal{E}'(\mathbb{R}^2)$.

Filtered backprojection is an efficient, fast reconstruction method that is easily implemented [66] by using an approximation to the operator Λ_p that is convolution with a function (see, e.g., [65] or [84]). Note that FBP requires data over all lines through the object—it is not local: in order to find $f(x)$, one needs data $\mathcal{R}_L f$ over all lines in order to evaluate $\Lambda_p \mathcal{R}_L f$ (which involves a Fourier transform).

To see the how sensitive FBP is to the number of the angles used in the reconstructions, we show reconstruction using 18, 36, and 180 angles. One can see that using too few angles creates artifacts. An optimal choice of angles and values of p can be determined using sampling theory [65, 14, 13].

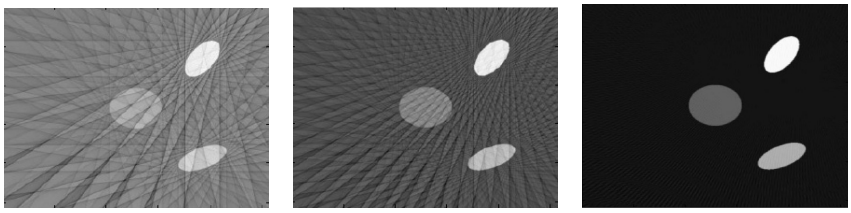

Fig. 1.8. FBP reconstructions of phantom consisting of three ellipses. The left reconstruction uses 18 angles, the middle 36 angles, and the right one 180 angles.

Proof (Proof of Theorem 9). Let $f \in \mathcal{S}(\mathbb{R}^2)$. We write the two-dimensional Fourier inversion formula in polar coordinates.

$$f(x) = \frac{1}{2(2\pi)} \int_{\omega\in S^1} \int_{\tau\in\mathbb{R}} e^{ix\cdot(\tau\omega)} \widehat{f}(\tau\omega)|\tau| \, \mathrm{d}\tau \, \mathrm{d}\omega \tag{1.19}$$

$$= \frac{1}{4\pi} \int_{\omega\in S^1} \int_{\tau\in\mathbb{R}} \frac{e^{i\tau(\omega\cdot x)}}{\sqrt{2\pi}} |\tau| \left(\mathcal{F}_p \mathcal{R}_L f\right)(\omega,\tau) \, \mathrm{d}\tau \, \mathrm{d}\omega \tag{1.20}$$

$$= \frac{1}{4\pi} \int_{\omega\in S^1} \left(\Lambda_p \mathcal{R}_L f\right)(\omega, \omega\cdot x) \, \mathrm{d}\omega = \frac{1}{4\pi} \mathcal{R}_L^* \Lambda_p \mathcal{R}_L f(x) \, . \tag{1.21}$$

The factor of $1/2$ in front of the integral in (1.19) occurs because the integral is over $\tau \in \mathbb{R}$ rather than $\tau \in [0,\infty)$. In (1.20), we use the Fourier Slice Theorem (Theorem 2), and in (1.21) we use the definitions of Λ_p and of $\mathcal{R}_L^*$. All of the integrals above exist because f, $\mathcal{F}f$, and $\mathcal{R}_L f$ are all rapidly decreasing at infinity.

We now explain why the FBP formula is valid for $f \in \mathcal{E}'(\mathbb{R}^2)$.

If $g(\omega,p)$ is a distribution of compact support, then we claim $\Lambda_p g$ is a tempered distribution. This is true since g has compact support. Therefore, its Fourier transform is polynomially increasing and smooth [83]. So, $|\tau| \, \mathcal{F}_p g(\omega,\tau)$ is a polynomially increasing continuous function and therefore in $\mathcal{S}'(S^1\times\mathbb{R})$. Since the inverse Fourier transform maps $\mathcal{S}'$ to $\mathcal{S}'$, $\Lambda_p g$ is a distribution in $\mathcal{S}'(S^1\times\mathbb{R})$.

Now, since $f\in\mathcal{E}'(\mathbb{R}^2)$, $\mathcal{R}_L f$ is a distribution of compact support on $S^1\times\mathbb{R}$ and so $\Lambda_p\mathcal{R}_L f$ is a distribution in $\mathcal{S}'(S^1\times\mathbb{R})$. By duality with $\mathcal{S}$, $\mathcal{R}_L^* : \mathcal{S}'(S^1\times\mathbb{R}) \to \mathcal{S}'(\mathbb{R}^2)$, so $\mathcal{R}_L^*\Lambda_p\mathcal{R}_L f$ is defined for $f\in\mathcal{E}'(\mathbb{R}^2)$. The Fourier Slice Theorem holds for f [42] so the FBP formula can be proved for f as is done above for $\mathcal{S}$ (see [24] more generally). □

1.3.5 Limited Data Algorithms

In limited data problems some data are missing, and we now go through several methods for limited data problems including ROI CT, limited angle CT, and limited angle ROI CT.

ROI Tomography

Lambda Tomography [15, 16, 93] is an effective easy to implement algorithm for ROI CT. The fundamental idea is to replace Λ_p by $-d^2/dp^2$ in the FBP formula. The relation between these two operators is that $\Lambda_p^2 = -d^2/dp^2$, which will be justified in Example 9. This motivates the definition

$$\mathcal{L}_x f := \frac{1}{4\pi} \mathcal{R}_L^* \left(-\frac{d^2}{dp^2} \mathcal{R}_L f \right) . \tag{1.22}$$

The advantage is that $\mathcal{L}_x$ is local in the following sense. To calculate $\mathcal{L}_x f$, one needs the values of $\left(-d^2/dp^2\right)\mathcal{R}_L f$ at all lines through x (since $\mathcal{R}_L^*$ evaluated at x integrates over all such lines). Furthermore, $\left(-d^2/dp^2\right)$ is a local operator and to calculate $\left(-d^2/dp^2\right)\mathcal{R}_L f$ at a line through x, one needs only data $\mathcal{R}_L f$

over lines close to x. Therefore, one needs only data over all lines near x to calculate $\mathcal{L}_x f$; thus $\mathcal{L}_x$ can be used on ROI data. Although Lambda CT reconstructs $\mathcal{L}_x f$, not f itself, it shows boundaries very clearly [15].

Kennan Smith developed an improved local operator that shows contours of objects, not just boundaries. His idea was to add a positive multiple of $\mathcal{R}_L^* \mathcal{R}_L f$ to the reconstruction to get

$$\mathcal{L}_{x,\mu} f = \frac{1}{4\pi} \mathcal{R}_L^* \left(\left(-\frac{d^2}{dp^2} + \mu \right) \mathcal{R}_L f \right) \tag{1.23}$$

for some $\mu > 0$. Using (1.35) one sees that

$$\mathcal{R}_L^* \left(\mu \mathcal{R}_L f \right)(x) = \left(\frac{2\mu}{\|x\|} * f \right)(x), \tag{1.24}$$

so this factor adds contour to the reconstruction since the convolution with $2\mu/\|x\|$ emphasizes the values of f near x. Lambda reconstructions look much like FBP reconstructions even though they are local. A discussion of how to choose μ to counteract a natural cupping effect of $\mathcal{L}_x$ is given in [15]. This operator is local for the same reasons as $\mathcal{L}_x$ is, and it was used in the ROI reconstruction in Figure 1.4.

Lambda CT can be adapted to a range of limited data problems including limited angle tomography(e.g., [55, 50]), exterior tomography [76], and three dimensional problems such as cone beam CT [48, 2, 97, 23] and conical tilt electron microscopy [21]. We now talk about one such application.

Limited Angle CT

There are several algorithms for limited angle tomography (e.g., [3, 12, 60, 50, 98]), and we will discuss ones that are simple generalizations of FBP and Lambda CT. The key to each is to use the limited angle backprojection operator that uses angles in an interval (a, b) with $b - a < \pi$

$$\mathcal{R}_{L,\lim}^* g(x) = \int_{\varphi=a}^{b} g(\omega(\varphi), x \cdot \omega(\varphi)) \mathrm{d}\varphi \,. \tag{1.25}$$

The limited angle FBP and limited angle Lambda algorithms are

$$\mathcal{R}_{L,\lim} \Lambda_p \mathcal{R}_L f \quad \text{and} \quad \mathcal{R}_{L,\lim} \left(-\frac{d^2}{dp^2} \right) \mathcal{R}_L f \tag{1.26}$$

respectively. The objects in Figure 1.3 are reconstructed using this limited angle FBP algorithm. Limited angle Lambda CT is local so it can be used for the limited angle ROI data in electron microscope tomography [77, 80].

1.3.6 Fan Beam and Cone Beam CT

The parallel beam parameterization we use of lines in the plane is more convenient mathematically, but modern CT scanners use a single X-ray source that emits X-rays in a fan or cone beam. The source and detectors (on the other side of the body) move around the body and quickly acquire data. This requires a different parameterization of lines, the so-called *fan beam parameterization*, if the X-rays are collimated to one reconstruction plane. Let C be the curve of sources (typically a circle or helix surrounding the specimen), and let $(\omega, \theta) \in C \times S^1$. Then,

$$L(\omega, \theta) = \{\omega + t\theta \,:\, t > 0\}$$

is the ray starting at ω in direction θ, and the *cone beam line transform* is

$$\mathcal{C}f(\omega, \theta) = \int_{t=0}^{\infty} f(\omega + t\theta)\, \mathrm{d}t.$$

In this case the analogues of the formulas we proved are a little more complicated. For example, the Lambda operator can be calculated by taking the negative second derivative in $\theta \in S^1$. The other formulas are similar and one can find them in [87, 65].

In cone beam tomography, the source is collimated to illuminate a cone in space. This images a volume in the body, rather than a planar region as $\mathcal{R}_L$ and the fan beam transform do. However, the reconstruction formulas are more subtle [51, 23].

These data acquisition methods have several advantages over parallel beam data acquisition. First, the scanners are simpler and acquire data more quickly than old style parallel beam scanners since the fan beam X-ray source and detector array move in a circle around the object. The original CT scanners took data using the parallel geometry, and so a single X-ray source and detector were translated to get data over parallel lines in one direction and then the source and detector were rotated to get lines for other angles.

This is all discussed in Herman's Chapter in this book [41].

1.3.7 Algorithms in Conical Tilt ET

Conical tilt ET [102] is a new data acquisition geometry in ET that has the potential to provide faster data acquisition as well as clearer reconstructions. We will briefly review the algorithms we used for the conical tilt ET reconstructions in Section 1.2.2. This will lay the groundwork to understand why the reconstructions in that section from two very similar algorithms are so dramatically different. The model and mathematics are fully discussed in Öktem's chapter in this book [69].

First we provide notation. For $\omega \in S^2$, we denote the plane through the origin perpendicular to ω by

$$\omega^P = \{x \in \mathbb{R}^3 \,:\, x \cdot \omega = 0\}. \tag{1.27}$$

The tangent space to the sphere S^2 is

$$T(S^2) = \{(\omega, x) \,:\, \omega \in S^2, x \in \omega^P\}$$

since the plane ω^P is the tangent plane to S^2 at ω. This gives the *parallel beam* parameterization of lines in space: for $(\omega, x) \in T(S^2)$, the line

$$L(\omega, x) = \{x + t\omega \,:\, t \in \mathbb{R}\}.$$

If ω is fixed, then the lines $L(\omega, x)$ for $x \in \omega^P$ are all parallel. As noted in Öktem's chapter in this book [69], ET data are typically taken on a curve $S \subset S^2$. This means the lines in the data set are parameterized by

$$\mathcal{M}_S = \{(\omega, x) \,:\, \omega \in S, x \in \omega^P\}.$$

So, for $f \in L^1(\mathbb{R}^3)$, the ET data of f for lines parallel S can be modeled as the *parallel beam transform*

$$\mathcal{P}_S f(\omega, x) = \int_{t \in \mathbb{R}} f(x + t\omega)\, \mathrm{d}t \quad \text{for } (\omega, x) \in \mathcal{M}_S.$$

Its dual transform is defined for functions g on $\mathcal{M}_S$ as

$$\mathcal{P}_S^* g(x) = \int_{\omega \in S} g(\omega, x - (x \cdot \omega)\omega) \mathrm{d}\omega,$$

where $\mathrm{d}\omega$ is the arc length measure on S. This represents the integral of g over all lines through x.

In this section, we consider conical tilt ET in which an angle $\alpha \in (0, \pi/2)$ is chosen and data are taken for angles on the latitude circle

$$S_\alpha = \{(\sin(\alpha)\cos(\varphi), \sin(\alpha)\sin(\varphi), \cos(\alpha))\} \,:\, \varphi \in [0, 2\pi]\}.$$

Let C_α be the vertical cone with vertex at the origin and opening angle α:

$$C_\alpha = \{t\omega \,:\, \omega \in S_\alpha\}.$$

Note that C_α is the cone generated by S_α.

We describe the two algorithms for which reconstructions were given in Section 1.2.2. The first algorithm is a generalization of one developed for cone beam CT by Louis and Maaß [61]:

$$\mathcal{L}_\Delta f = \mathcal{P}_S^*(-\Delta_S)\mathcal{P}_S f, \tag{1.28}$$

where Δ_S is the Laplacian on the detector plane, ω^P. We also define the operator

$$\mathcal{L}_S f = \mathcal{P}_S^*(-\mathcal{D}_S)\mathcal{P}_S f, \tag{1.29}$$

where $\mathcal{D}_S$ is the second derivative on the detector plane ω^P in the tangent direction to the curve S at ω (see Öktem's chapter in this book [69]). To better understand these operators, we will write them as convolution operators.

Theorem 10. *Let $\mathcal{P}_S$ be the conical tilt ET transform with angle $\alpha \in (0, \pi/2)$. Let $f \in \mathcal{E}'(\mathbb{R}^3)$. Then*

$$\mathcal{P}_S^* \mathcal{P}_S f = f * I = \int_{y \in C_\alpha} \frac{f(x+y)}{\|y\|} \mathrm{d}y \tag{1.30}$$

$$\mathcal{L}_\Delta f = (-\Delta)(f * I) \tag{1.31}$$

$$\mathcal{L}_S f = \left(-\Delta + \csc^2(\alpha) \frac{\partial^2}{\partial z^3}\right) f * I \tag{1.32}$$

where I is the distribution defined, for $f \in \mathcal{D}(\mathbb{R}^2)$ by

$$I(f) = \int_{y \in C_\alpha} f(y) \frac{1}{\|y\|} \mathrm{d}y$$

and $\mathrm{d}y$ is the surface area measure on the cone C_α.

Equation (1.30) makes sense since $\mathcal{P}_S^*$ integrates $\mathcal{P}_S f$ over all lines in the data set through x, and these are exactly the lines in the shifted cone $x + C_\alpha$. The theorem shows that each of the operators are related to a simple convolution with a singular weighted integration over the cone C_α.

Proof. We first prove the theorem for $f \in \mathcal{D}(\mathbb{R}^3)$, and we calculate (1.30):

$$\begin{aligned} \mathcal{P}_S^* \mathcal{P}_S f(x) &= \int_{\omega \in S} \int_{t \in \mathbb{R}} f(x - (x \cdot \omega)\omega + t\omega) \mathrm{d}t \, \mathrm{d}\omega \\ &= \int_{\omega \in S} \int_{t \in \mathbb{R}} f(x + s\omega) \, \mathrm{d}s \, \mathrm{d}\omega \end{aligned}$$

where we made the substitution $s = t - (x \cdot \omega)$. Now, we convert this to an integral over C_α:

$$\begin{aligned} \mathcal{P}_S^* \mathcal{P}_S f(x) &= \int_{\omega \in S} \int_{s \in \mathbb{R}} f(x + s\omega) \frac{1}{|s|} \, |s| \, \mathrm{d}s \mathrm{d}\omega \\ &= \int_{y \in C_\alpha} \frac{f(x+y)}{\|y\|} \mathrm{d}y \end{aligned}$$

since the measure on the cone C_α is $dy = |s| \, ds \, \mathrm{d}\omega$ where $y = s\omega$.

To prove (1.31), one moves Δ inside the integral. Then one uses rotation invariance of Δ (to write Δ in coordinates

$$(s, t, p) \mapsto (s\omega + t\omega' + p\omega \times \omega')$$

where ω' is the unit vector in the tangent to S at ω and in direction of increasing φ). Finally, one uses an integration by parts to show that $\mathcal{P}_S^*$ intertwines Δ and Δ_S. To prove (1.32), one uses (1.31) and a calculation to show that $\left(-\Delta + \csc^2(\alpha) \frac{\partial^2}{\partial z^2}\right)$ and $\mathcal{D}_S$ are intertwined by $\mathcal{P}_S^*$.

Finally, let $f \in \mathcal{E}'(\mathbb{R}^3)$. Since f has compact support, the convolution $f * I$ is defined by [83, 6.37 Theorem]. Then, the rest of the proof uses the fact that the equalities are true for $f \in \mathcal{D}(\mathbb{R}^3)$ and continuity of the operators (since $\mathcal{P}_S$ is a Fourier integral operator, which will be discussed in Section 1.5.3). □

1.4 Microlocal Analysis

Now that we have seen some differences in reconstructions we will develop deep mathematics to understand those differences. The key is that we were evaluating each reconstruction depending on which singularities or boundaries of objects they imaged properly and when artifacts were added in some cases.

1.4.1 Singular support and Wavefront Set

Definition 1. *Let $u \in \mathcal{D}'(\Omega)$. The singular support of u, denoted by* $\operatorname{ssupp}(u)$ *is the complement in Ω of the largest open set on which u is C^∞ smooth.*

In other words, we say a point $x_0 \in \Omega$ is not in the singular support of u if u is smooth in a neighborhood of x_0. Let us consider some examples.

Example 3. Consider the square $S = [0,1]^2$ in $\mathbb{R}^2$. Let f be the characteristic function,

$$u(x,y) = \begin{cases} 1 & \text{if } (x,y) \in S; \\ 0 & \text{otherwise.} \end{cases} \tag{1.33}$$

Then $\operatorname{ssupp}(u)$ is the boundary of the square because that is where u is not smooth; see Figure 1.9.

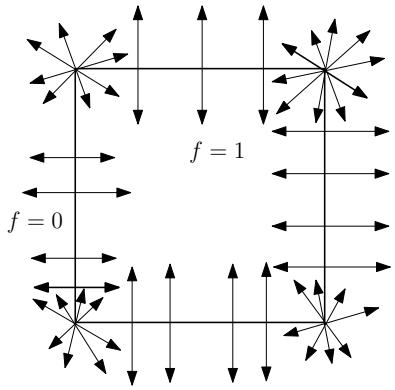

Fig. 1.9. The function $f = 1$ in the interior of the square and $f = 0$ in the complement. The singular support, $\operatorname{ssupp}(f)$, is the boundary of the rectangle, and the wavefront set directions are shown in the figure.

Smoothness of a distribution u (we will assume $u \in \mathcal{E}'(\Omega)$) is related to the rapid decay of the Fourier transform of u. We recall the following definition:

Definition 2. *We say a function $f : \mathbb{R}^n \to \mathbb{C}$ is* rapidly decaying at infinity *if for every $N \geqslant 0$, there is a C_N such that $|f(x)| \leqslant C_N(1 + \|x\|)^{-N}$ for all $x \in \mathbb{R}^n$.*

Theorem 11 ([83]). *A distribution $u \in \mathcal{E}'(\Omega)$ is in $C_c^\infty(\Omega)$ if and only if its Fourier transform is rapidly decaying at infinity.*

This theorem implies that if a distribution u is not C^∞ smooth, then there are non-zero frequency directions ξ such that the Fourier transform $\widehat{u}$ does not satisfy the estimate of Theorem 11 in any conic neighborhood Γ containing ξ. However, this is global information; it does not yet relate to singular support—the points where u is not smooth. To make this connection, we need to consider directions near which a localized Fourier transform of u does not satisfy these estimates. This leads us to the concept of C^∞ wavefront set.

Definition 3. *Let u be a distribution defined on an open set $\Omega \subset \mathbb{R}^n$. We say that $(x_0, \xi_0) \in \Omega \times \mathbb{R}^n \backslash \mathbf{0}$ is* not *in the wavefront set of u, if there is a $\psi \in C_c^\infty(X)$ identically 1 near x_0 and an open cone Γ containing ξ_0 such that given any N, there is a C_N such that*

$$\left|\widehat{\psi u}(\xi)\right| \leqslant C_N(1 + \|\xi\|)^{-N} \text{ for } \xi \in \Gamma.$$

The C^∞ wavefront set of a distribution u will be denoted by $\mathrm{WF}(u)$.

Remark 1. To be more precise, we view elements of the wavefront set to be elements of the cotangent bundle $T^*\Omega\backslash\mathbf{0}$ using the notation

$$\xi \mathrm{d}x = \xi_1 \mathrm{d}x_1 + \cdots + \xi_n \mathrm{d}x_n \text{ for } \xi \in \mathbb{R}^n \backslash \mathbf{0}.$$

Through this, one can make sense of wavefront sets for distributions on manifolds.

Note that the cutoff function, ψ, in this definition is somewhat more restrictive than what is sometimes given (just that $\psi(x_0) \neq 0$) but it is equivalent [45].

Theorem 12 ([45]). *Let u be a distribution defined on an open set $\Omega \subset \mathbb{R}^n$ and π_x denote the x-projection* $\mathrm{WF}(u)$. *Then* $\pi_x\left(\mathrm{WF}(u)\right) = \mathrm{ssupp}(u)$.

Example 4. Consider the Dirac delta distribution δ_0 in $\mathbb{R}^n$. Then $\mathrm{ssupp}(\delta_0) = \{0\}$ because δ_0 is zero away from the origin and supported at the origin. So, by Theorem 12, $x = 0$ is the only point above which there can be wavefront set. Furthermore, if ψ is a cutoff function at $x_0 = 0$, then $\mathcal{F}(\psi\delta_0) = 1/(2\pi)^{n/2}$, so $\mathrm{WF}(\delta_0) = \{(0, \xi \mathrm{d}x), \xi \neq 0\}$.

Example 5. We will now show for the f given in Example 3 that $\mathrm{WF}(f)$ consists of the non-zero normal directions at all the singular support points except the four corner points. At these corner points all non-zero directions are in the wavefront set, as illustrated in Figure 1.9.

Consider first a non-corner point x_0 in the singular support We can assume that this point is on the x-axis, $x_0 = (a, 0)$ where $a \in (0, 1)$. Fix a direction

$\xi^0 = (\xi_1^0, \xi_2^0)$ with $\xi_1^0 \neq 0$. We will show that the localized Fourier transform is rapidly decaying in a conic neighborhood of ξ^0. We can find a narrow conic neighborhood Γ containing ξ^0 such $|\xi_1| \geqslant c\,\|\xi\|$ for some $c > 0$ and all $\xi \in \Gamma$ (here $\xi = (\xi_1, \xi_2)$). Let $\varphi \in C_c^\infty(\mathbb{R}^2)$ be a function of the form $\varphi(x_1, x_2) = \varphi_1(x_1)\varphi_2(x_2)$ that is identically 1 near x_0. Without loss of generality, we may assume φ_1 is even about a and φ_2 is even about 0. Consider

$$\widehat{\varphi f}(\xi) = \frac{1}{\sqrt{2\pi}} \int_{-\infty}^{\infty} e^{-\mathrm{i}x_1\cdot\xi_1} \varphi_1(x_1)\mathrm{d}x_1 \frac{1}{\sqrt{2\pi}} \int_0^{\infty} e^{-\mathrm{i}x_2\xi_2} \varphi_2(x_2)\mathrm{d}x_2\,.$$

Denote the left-hand integral in this expression by $L(\xi_1)$ and the right-hand integral by $R(\xi_2)$. Note that the R is bounded in ξ_2 because the integrand is uniformly bounded and of compact support. Because φ_1 is in $\mathcal{S}(\mathbb{R})$, $L(\xi_1)$ is also in $\mathcal{S}(\mathbb{R})$, since it is the one-dimensional Fourier transform of φ_1. Therefore $L(\xi_1)$ is rapidly decaying at infinity as a function of ξ_1. Since $|\xi_1| > c\,\|\xi\|$ in Γ, the function $\xi \mapsto L(\xi_1)$ decays rapidly at infinity for ξ in Γ. Since R is bounded, we see that $\widehat{\varphi f}(\xi)$ decays rapidly in Γ. This shows that the only possible vectors in $\mathrm{WF}(f)$ above $x_0 = (a, 0)$ are vertical ones.

Since f is not smooth at x_0, at least one vertical vector at x_0 must be in $\mathrm{WF}(f)$ by Theorem 11. Therefore, $R(\xi_2)$ must not rapidly decay in either the positive direction ($\xi_2 > 0$) or the negative direction. Since φ_2 is an even function in $\mathcal{S}(\mathbb{R})$, $\mathcal{F}(\varphi_2)(\xi_2) = R(\xi_2) + R(-\xi_2)$ is rapidly decreasing at $\pm\infty$, so $R(\xi_2)$ must *not* be rapidly decaying for $\xi_2 > 0$ *and* for $\xi_2 < 0$ (since $R(\xi_2)$ is not rapidly decaying in at least one direction and the sum is rapidly decaying in both positive and negative directions). Therefore, both vertical vectors are in $\mathrm{WF}(f)$ at x_0. (In another proof, one shows $R(\xi_2) = \mathcal{O}(1/|\xi_2|)$ by performing two integrations by parts on that integral.)

We now show all directions are in $\mathrm{WF}(f)$ above $(0, 0)$. We use symmetric cutoffs in x_1 and x_2 at 0. Then

$$\widehat{\varphi f}(\xi) = \frac{1}{\sqrt{2\pi}} \int_0^{\infty} e^{-\mathrm{i}x_2\xi_2} \varphi_2(x_2)\mathrm{d}x_2 \frac{1}{\sqrt{2\pi}} \int_0^{\infty} e^{-\mathrm{i}x_1\cdot\xi_1} \varphi_1(x_1)\mathrm{d}x_1.$$

The proof for $R(\xi_2)$ above can be used to show that neither integral decays rapidly at infinity in this case. This shows that $\mathrm{WF}(\varphi f)$ consists of all directions at $x_0 = 0$. The proofs at the other corners are similar.

Example 6. If f is the characteristic function of a set, Ω with a smooth boundary, then $\mathrm{WF}(f)$ is the conormal bundle

$$N^*(\Omega) = \{(x, \xi\mathrm{d}x) \,:\, x \in \mathrm{bd}(\Omega),\ \xi \text{ is normal to } \mathrm{bd}(\Omega) \text{ at } x\}$$

This is suggested by Example 5 and it follows from results in [45].

If f is a linear combination of characteristic functions of sets with smooth boundary, then $\mathrm{WF}(f)$ is the union of the normal sets of the individual sets unless cancellation occurs along shared boundaries.

1.4.2 Pseudodifferential Operators

To motivate the definition of these operators, we start with an example.

Theorem 13. *For $f \in \mathcal{S}(\mathbb{R}^2)$,*

$$\mathcal{R}_L^* \mathcal{R}_L u(x) = \int e^{\mathrm{i}x\cdot\xi} \frac{2}{\|\xi\|} \widehat{u}(\xi) \mathrm{d}\xi = \frac{1}{\pi} \int e^{\mathrm{i}(x-y)\cdot\xi} \frac{1}{\|\xi\|} u(y) \mathrm{d}y \mathrm{d}\xi \,. \tag{1.34}$$

Proof. Using a polar integration about x one shows that

$$\mathcal{R}_L^* \mathcal{R}_L f = f * \frac{2}{\|x\|} \,. \tag{1.35}$$

Then, since $\mathcal{F}\left(1/\|x\|\right) = 1/\|\xi\|$ [40, Lemma 6.2, p. 238], we see that

$$\mathcal{R}_L^* \mathcal{R}_L u = \mathcal{F}^{-1}\mathcal{F}\left(u * \frac{2}{\|x\|}\right) = \mathcal{F}^{-1}\left(2\pi \frac{2}{\|\xi\|} \widehat{u}\right)$$

using the fact that the Fourier transform of a convolution in $\mathbb{R}^2$ (with our normalization) is the product of the Fourier transforms times 2π. Writing $\mathcal{F}^{-1}$ as an integral in the right-hand expression proves the theorem. □

We should point out that the left-hand integral in (1.34) converges for $f \in \mathcal{S}(\mathbb{R}^2)$, but the right-hand integral in (1.34) does not converge. However, one can do integrations by parts at infinity to make it converge for $f \in \mathcal{S}(\mathbb{R}^2)$ or $f \in \mathcal{E}'(\mathbb{R}^2)$ for pseudodifferential operators (e.g., [72]).

With this as model, we consider operators with integral representation

$$\mathcal{P}u(x) = \int e^{\mathrm{i}(x-y)\cdot\xi} p(x,y,\xi) u(y) \mathrm{d}y \mathrm{d}\xi \tag{1.36}$$

The study of the operator $\mathcal{P}$ is important in imaging for the following reasons:

1. Assuming p satisfies certain estimates (see Definition 4), we can describe precisely the action of $\mathcal{P}$ on the singularities or the sharp changes of u.
2. If we have a procedure to invert or approximately invert the operator $\mathcal{P}$ by another operator $\mathcal{Q}$ having a similar integral representation as that of $\mathcal{P}$, then by (a), we would have that the singularities of $\mathcal{Q}\mathcal{P}u$ are identical to those of u. We see that through this approximate inversion process, we have a procedure to recover the singularities or the sharp changes of u.

An operator $\mathcal{P}$ of the form (1.36) with p satisfying certain estimates is called a *pseudodifferential operator* (ΨDO) [31, 91, 45, 86, 90]. We define this below (see Definition 5).

In order to motivate the appropriate conditions and estimates that p should satisfy, let us look at the following simple example:

Consider a linear partial differential operator of the form,

$$\mathcal{P}(x,D) = \sum_{|\nu|\leqslant m} a_\nu(x) D_x^\nu. \tag{1.37}$$

Here $\nu = (\nu_1, \cdots, \nu_n)$ is a multi-index and

$$D_x^\nu = (-i)^{(\nu_1+\cdots+\nu_n)} \frac{\partial^{\nu_1}}{\partial x_1^{\nu_1}} \cdots \frac{\partial^{\nu_n}}{\partial x_n^{\nu_n}}.$$

For simplicity let u be a compactly supported function. Applying the Fourier transform,

$$\widehat{D_x^\nu u}(\xi) = \frac{1}{(2\pi)^{n/2}} \int e^{-ix\cdot\xi} D_x^\nu u(x) \mathrm{d}x. \tag{1.38}$$

Integrating by parts $|\nu|$ times, we obtain,

$$\widehat{D_x^\nu u}(\xi) = \xi^\nu \widehat{u}(\xi). \tag{1.39}$$

With this we have

$$\mathcal{P}(x,D)u(x) = \frac{1}{(2\pi)^{n/2}} \int e^{\mathrm{i}(x-y)\cdot\xi} p(x,\xi) u(y) \mathrm{d}y \mathrm{d}\xi \tag{1.40}$$

where

$$p(x,\xi) = \sum_\nu a_\nu(x) \xi^\nu.$$

The function $p(x,\xi)$ is called the *symbol* of the partial differential operator (PDO), $\mathcal{P}(x,D)$.

The function $p(x,\xi)$ satisfies the following property: Differentiating p with respect to ξ^α lowers the degree with respect to ξ of the resulting function by $|\alpha|$, whereas differentiating with respect to x^β for any multi-index β does not alter the degree of homogeneity with respect to ξ of the resulting function.

More precisely we have the following estimate:

Let α and β be any multi-index. For x in a bounded subset of $\mathbb{R}^n$, there is a constant C such that

$$\left|\partial_\xi^\alpha \partial_x^\beta p(x,\xi)\right| \leqslant C(1+\|\xi\|)^{m-|\alpha|}. \tag{1.41}$$

Here m is the order of the PDO, $\mathcal{P}(x,D)$. In order to get this inequality, we first rewrite the terms of $p(x,\xi)$ by combining terms of the same homogeneous degree with respect to the ξ variable.

Differentiate ξ^ν α times with respect to $\xi_1, \cdots, \xi_n$, where the number of times we differentiate ξ^ν with respect to a particular ξ_l depends on α_l. We see that this reduces the degree of homogeneity of ξ^ν by $|\alpha|$ and the highest order terms dominate. On a bounded subset of $\mathbb{R}^n$, all derivatives of the a_ν are bounded. This gives the estimate (1.41).

Now we can generalize the class of operators that have Fourier integral representations of the form (1.40) by admitting a larger class of functions

$p(x,\xi)$ to be symbols. We consider those functions p that satisfy the estimate as in (1.41) and that behave like polynomials or the inverse of polynomials in ξ as $\|\xi\| \to \infty$. In other words, we want $p(x,\xi)$ to grow or decay in powers of $\|\xi\|$ and differentiation with respect to ξ lowers the order of growth or raises the order of decay. Furthermore, in order to include $\mathcal{R}_L^*\mathcal{R}_L$ in our class of operators (see Example 13), we allow some latitude at $\xi = 0$.

In the interest of flexibility, we will also let the function p depend on x, y and ξ. We will denote such functions as *amplitudes* [31, 91, 45, 86, 90].

Definition 4. *Let $X \subset \mathbb{R}^n$ be an open subset. An amplitude of order m is a function that satisfies the following properties:*

1. *$p(x,y,\xi) \in C^\infty(X \times X \times \mathbb{R}^n \backslash \{0\})$,*
2. *For every compact set K and for multi-index α, β, γ,*
   a) there is a constant $C = C(K,\alpha,\beta,\gamma)$ such that

$$\left|D_\xi^\alpha D_x^\beta D_y^\gamma p(x,y,\xi)\right| \leqslant C(1+\|\xi\|)^{m-|\alpha|} \quad \text{for } \|\xi\| > 1, \text{ and}$$

   b) $p(x,y,\xi)$ is locally integrable for x and y in K and $\|\xi\| \leqslant 1$.

It is important to note that in Definition 4, p need not be a polynomial in ξ and m can be any real number. The local integrability condition can be relaxed if p is a sum of homogeneous terms in ξ [72].

Now let us define pseudodifferential operators.

Definition 5. *Let $X \subset \mathbb{R}^n$ be an open subset. A pseudodifferential operator (ΨDO) is an operator of the form,*

$$\mathcal{P}u(x) = \frac{1}{(2\pi)^n} \int e^{\mathrm{i}(x-y)\cdot\xi} p(x,y,\xi) u(x) \mathrm{d}y \mathrm{d}\xi,$$

where $p(x,y,\xi)$ is a function that satisfies the properties of Definition 4.

The operator $\mathcal{P}$ has order m if its symbol is of order m, and $\mathcal{P}$ is elliptic of order m if for each compact set $K \subset \Omega$, there is a constant $C_K > 0$ such that for x and y in K and $\|\xi\| \geqslant C_K$

$$|p(x,y,\xi)| \geqslant C_K(1+\|\xi\|)^m . \tag{1.42}$$

The next theorem highlights two fundamental properties of ΨDOs.

Theorem 14 (Pseudolocal Property [91]). *If $\mathcal{P}$ is a ΨDO, then $\mathcal{P}$ satisfies the* pseudolocal property*:*

$$\operatorname{ssupp}(\mathcal{P}u) \subset \operatorname{ssupp}(u) \text{ and } \operatorname{WF}(\mathcal{P}u) \subset \operatorname{WF}(u) .$$

If, in addition, $\mathcal{P}$ is elliptic, then

$$\operatorname{ssupp}(\mathcal{P}u) = \operatorname{ssupp}(u) \text{ and } \operatorname{WF}(\mathcal{P}u) = \operatorname{WF}(u) .$$

Note that, although ΨDOs can spread out the support of the function u, they do not spread out its singular support. Elliptic ΨDOs preserve singular support and wavefront set.

Equation (1.34) shows that the composition $\mathcal{R}_L^*\mathcal{R}_L$ is a pseudodifferential operator since its symbol $(4\pi)/\|\xi\|$ satisfies the conditions in Definition 4. Furthermore, because the symbol satisfies the ellipticity estimate (1.42), $\mathcal{R}_L^*\mathcal{R}_L$ is an elliptic ΨDO of order -1.

Example 7. We now express powers of d/dp and Δ as ΨDOs.

According to (1.40), the symbol of $-d^2/dp^2$ is $|\tau|^2$ where τ is the dual variable to p. So, the symbol of $\sqrt{-d^2/dp^2}$ should be $|\tau|$. The rationale is that, if one calculates

$$\begin{aligned} -\frac{d^2}{dp^2} f &= \mathcal{F}^{-1} |\tau|^2 \mathcal{F} f = \mathcal{F}^{-1} |\tau| \mathcal{F} \left(\mathcal{F}^{-1} |\tau| \mathcal{F} f \right) \\ &= \sqrt{-\frac{d^2}{dp^2}} \circ \sqrt{-\frac{d^2}{dp^2}} f \,. \end{aligned} \tag{1.43}$$

This justifies why

$$\Lambda_p = \sqrt{-d^2/dp^2} \,. \tag{1.44}$$

Since

$$-\Delta = D_{x_1}^2 + \cdots + D_{x_n}^2 \,,$$

its symbol is $\|\xi\|^2$. Using the symbol for Δ in (1.40), we can easily define powers of the Laplacian. For example, $\sqrt{-\Delta}$ will have symbol $\|\xi\|$ and Fourier representation

$$\sqrt{-\Delta} u = \frac{1}{(2\pi)^n} \int e^{\mathrm{i}(x-y)\cdot\xi} \|\xi\| \, u(y) \mathrm{d}y \mathrm{d}\xi$$

and $(-\Delta)^{-1/2}$ has symbol $1/\|\xi\|$

$$(-\Delta)^{-1/2} u = \frac{1}{(2\pi)^n} \int e^{\mathrm{i}(x-y)\cdot\xi} \frac{1}{\|\xi\|} u(y) \mathrm{d}y \mathrm{d}\xi.$$

Now, as a calculation in distributions using Fourier transforms (similar to (1.43)), one sees that $(-\Delta)^{-1/2} \circ \sqrt{-\Delta}$ is the identity map.

Note that $\sqrt{-d^2/dp^2}$, $\sqrt{-\Delta}$, $(-\Delta)^{-1/2}$ are all elliptic ΨDOs.

Example 8. The last example justified why the operator Λ_p is really $\sqrt{-d^2/dp^2}$. So, the FBP inversion formula (1.18) can be written

$$f = \frac{1}{4\pi} \mathcal{R}_L^* \left(\sqrt{-d^2/dp^2} \mathcal{R}_L f \right) \,. \tag{1.45}$$

Equation (1.34) shows that $\mathcal{R}_L^*\mathcal{R}_L = 4\pi (-\Delta)^{-1/2}$. Using the observation at the end of the last example, one obtains a different version of the Filtered Backprojection inversion formula for $\mathcal{R}_L$,

$$f = \frac{1}{4\pi}\sqrt{-\Delta}\mathcal{R}_L^*\mathcal{R}_L f\,. \tag{1.46}$$

These calculations can be justified for distributions of compact support [42, 40].

Example 9. We now explore the Lambda operators given in (1.22) and (1.23). To get the Lambda operator, $\mathcal{L}_x$, from the FBP operator, one replaces the $\sqrt{-d^2/dp^2}$ in (1.45) by its square, $-d^2/dp^2$.

Here is another way to understand Lambda tomography. By evaluating another $\sqrt{-\Delta}$ in (1.46), we see that

$$\sqrt{-\Delta}f = -\frac{1}{4\pi}\Delta\mathcal{R}_L^*\mathcal{R}_L f = \frac{1}{4\pi}\mathcal{R}_L^*\left(-\frac{d^2}{dp^2}\mathcal{R}_L f\right)$$

where the second equality holds because $\mathcal{R}_L^*$ intertwines $-\Delta$ and $-d^2/dp^2$ (this is proven using an argument similar to the intertwining argument in the proof of Theorem 10). Because $\mathcal{R}_L^*\mathcal{R}_L$ is an elliptic ΨDO with symbol $4\pi/\|\xi\|$, the symbol of $\mathcal{L}_{x,\mu}$ is

$$\|\xi\| + \frac{\mu}{\|\xi\|}$$

and it is elliptic of order one. Therefore, $\mathcal{L}_{x,\mu}$ and $\mathcal{L}_x$ (corresponding to $\mu = 0$) are both elliptic ΨDOs.

Lambda tomography does not reconstruct f but $\left((-\Delta)^{1/2} + \mu\right) f$. The natural question then is, how different is this from f. We have just established that $\mathcal{L}_x$ and $\mathcal{L}_{x,\mu}$ are elliptic ΨDOs. Therefore, by Theorem 14 this means that these operators recover $\operatorname{ssupp}(f)$ and $\operatorname{WF}(f)$.

1.4.3 Fourier Integral Operators

In our analysis thus far, we studied the composition of a generalized Radon transform with its adjoint. This composed operator, as we learned, is a pseudodifferential operator. Theorem 14 shows us how ΨDOs act on singularities and wavefront sets. In this section, we will study more general operators and learn how they change wavefront sets.

Example 10. Now we write $\mathcal{R}_L$ in a special Fourier representation.

$$\begin{aligned}\mathcal{R}_L f(\omega, p) &= \frac{1}{(2\pi)^{1/2}}\int_{\tau\in\mathbb{R}} e^{\mathrm{i}p\tau}\mathcal{F}_p\left(\mathcal{R}_L f\right)(\omega,\tau)\,\mathrm{d}\tau \\ &= \int_{\tau\in\mathbb{R}} e^{\mathrm{i}p\tau}\widehat{f}(\tau\omega)\mathrm{d}\tau \\ &= \int_{\tau\in\mathbb{R}}\int_{x\in\mathbb{R}^2} e^{\mathrm{i}(p-(x\cdot\omega))\tau}\frac{1}{2\pi}f(x)\mathrm{d}x\mathrm{d}\tau\,.\end{aligned} \tag{1.47}$$

The last expression in (1.47) looks like a ΨDO except that the τ and x integral are over different sets and the exponent is not the one for ΨDOs.

In many applications, it might be necessary to understand the properties of the Radon transform directly, rather than the composition with its adjoint. In our last example we saw that the Radon transform $\mathcal{R}_L$ had an integral representation of the form,

$$\mathcal{P}u(y) = \int e^{\mathrm{i}\phi(y,x,\xi)} p(y,x,\xi) u(x) \mathrm{d}x \mathrm{d}\xi. \tag{1.48}$$

The important differences between the operator $\mathcal{P}$ in (1.48) and a ΨDO are the following:

- The functions $\mathcal{P}u$ and u, in general, are functions on different sets Y and X, respectively. The spaces Y and X can be of different dimensions as well.
- The phase function is more general than that of a ΨDO, but is shares similar features. See Definition 6.
- The dimension of the frequency variable ξ can be different from that of the spaces Y and X, unlike as in the case of a ΨDO.

A simple example where an integral representation of (1.48) arises is when we use Fourier transform techniques to determine the solution to a constant coefficient wave equation:

$$\left(\partial_t^2 - \Delta_x\right) u = 0, \quad u(x,0) = 0, \quad \partial_t u(x,0) = g. \tag{1.49}$$

Now by taking Fourier transform in the space variable, we have the following integral representation for the solution to the wave equation,

$$u(x,t) = \frac{1}{2\mathrm{i}(2\pi)^n} \Big(\int e^{\mathrm{i}(x-y)\cdot\xi + t\|\xi\|} \frac{1}{\|\xi\|} g(y) \mathrm{d}y \mathrm{d}\xi \\ - \int e^{\mathrm{i}(x-y)\cdot\xi - t\|\xi\|} \frac{1}{\|\xi\|} g(y) \mathrm{d}y \mathrm{d}\xi \Big).$$

Note that the phase functions in the above solution are $\phi_\pm(x,y,\xi) = (x-y)\cdot\xi \pm t\|\xi\|$.

If $f : \mathbb{R}^n \to \mathbb{R}$, then we will use the notation

$$\partial_x f(x) = \frac{\partial f}{\partial x_1} \mathrm{d}x_1 + \cdots + \frac{\partial f}{\partial x_1} \mathrm{d}x_n$$

for the differential of f with respect to x. If g is a function of (φ, p) then

$$\partial_{\varphi,p} g(\varphi,p) = \frac{\partial g}{\partial \varphi} \mathrm{d}\varphi + \frac{\partial g}{\partial p} \mathrm{d}p$$

will denote the differential of g with respect to the variables (φ, p).

Definition 6. *Let $Y \subset \mathbb{R}^m$ and $X \subset \mathbb{R}^n$ be open subsets. A real valued function $\phi \in C^\infty(Y \times X \times \mathbb{R}^N \backslash \{0\})$ is called a phase function if*

1. *ϕ is positive homogeneous of degree* 1 *in* ξ. *That is* $\phi(y,x,r\xi) = r\phi(x,y,\xi)$ *for all* $r > 0$.
2. $(\partial_y\phi, \partial_\xi\phi)$ *and* $(\partial_x\phi, \partial_\xi\phi)$ *do not vanish for all* $(y,x,\xi) \in Y \times X \times \mathbb{R}^n \backslash \{0\}$.

Definition 7. *A Fourier integral operator (FIO)* $\mathcal{P}$ *is defined as*

$$\mathcal{P}u(y) = \int e^{i\phi(y,x,\xi)} p(y,x,\xi) u(x) \mathrm{d}x \mathrm{d}\xi,$$

where the amplitude $p(y,x,\xi) \in C^\infty(Y \times X \times \mathbb{R}^n)$ *and it satisfies the following estimate: For every compact set* $K \subset Y \times X$ *and for every multi-index* α, β, γ, *there is a constant* $C = C(K, \alpha, \beta, \gamma)$ *such that*

$$\left| D_\xi^\alpha D_x^\beta D_y^\gamma p(y,x,\xi) \right| \leqslant C(1 + \|\xi\|)^{m-|\alpha|} \text{ for all } x, y \in K \text{ and for all } \xi \in \mathbb{R}^n.$$

Finally, we define two important sets associated with this FIO.

$$\Sigma_\phi = \{(y,x,\xi) \in Y \times X \times (\mathbb{R}^n \backslash \mathbf{0}) \,:\, \partial_\xi \phi(y,x,\xi) = 0\}.$$

and the canonical relation

$$C := \{(y, \partial_y\phi(y,x,\xi); x, -\partial_x\phi(y,x,\xi)) : (y,x,\xi) \in \Sigma_\phi\}. \tag{1.50}$$

One can also include the local integrability condition 2b of Definition 4 for the amplitude of FIOs.

Note that $\mathcal{R}_L$ satisfies these conditions with phase function $\phi(\omega, p, x, \tau) = (p - x \cdot \omega)\tau$ and amplitude $p(y,x,\tau) = 1/(2\pi)$ so $\mathcal{R}_L$ is an FIO. Guillemin originally proved that a broad range of Radon transforms are FIOs [32, 33, 35]. We will study $\mathcal{R}_L$ more carefully in the next section.

Every ΨDO is an FIO with phase function $\phi(y,x,\xi) = (y-x)\cdot\xi$. However, $\mathcal{R}_L$ is a FIO that is not a ΨDO since its phase function is not of that form.

Definition 8. *Let* $C \subset T^*Y \times T^*X$, *and* $\widetilde{C} subset T^*X \times T^*Y$ *and* $A \subset T^*X$. *We define*

$$\begin{aligned} C \circ A = &\{(y, \eta \mathrm{d}y) \,:\, \exists\ (x, \xi \mathrm{d}x) \in A \text{ with } (y, \eta \mathrm{d}y; x, \xi \mathrm{d}x) \in C\} \\ \widetilde{C} \circ C = &\Big\{(\widetilde{x}, \widetilde{\xi} \mathrm{d}x; x, \xi \mathrm{d}x) \,:\, \exists\ (y, \eta \mathrm{d}y) \text{ with } (\widetilde{x}, \widetilde{\xi} \mathrm{d}x; y, \eta \mathrm{d}y) \in \widetilde{C}, \\ &\text{and } (y, \eta \mathrm{d}y; x, \xi \mathrm{d}x) \in C\Big\}. \end{aligned}$$

Theorem 15 ([45]). *Let* $\mathcal{P}$ *be an FIO and let* C *be the associated canonical relation. Then*

$$\mathrm{WF}(\mathcal{P}u) \subset C \circ \mathrm{WF}(u).$$

Example 11. In this example, we calculate the canonical relation of any ΨDO. First note that

$$\partial_x\phi = \xi \mathrm{d}x \quad \partial_y\phi = -\xi \mathrm{d}y \quad \partial_\xi\phi = (x-y)\mathrm{d}\xi.$$

Therefore, $\Sigma_\phi = \{(x, y, \xi) : x - y = 0\}$. Now, we use (1.50) and these calculations to see that the canonical relation for ΨDOs is

$$C = \{(x, \xi \mathrm{d}x; x, \xi \mathrm{d}x) : \xi \neq 0\}$$

which is the diagonal in $(T^*(\mathbb{R}^n)\backslash \mathbf{0})$ and which we denote by Δ. Using Theorem 15, we have that if $\mathcal{P}$ is a ΨDO, $\mathrm{WF}(\mathcal{P}u) \subset \mathrm{WF}(u)$.

We end this section with an important result on the wavefront set of the composition of two FIOs known as Hörmander-Sato Lemma.

Theorem 16 (Hörmander-Sato Lemma [45]). *Let $\mathcal{P}_1$ and $\mathcal{P}_2$ be two FIOs with canonical relations C_1 and C_2 respectively. Assume $\mathcal{P}_1 \circ \mathcal{P}_2$ is defined for distributions of compact support, and let u be a distribution of compact support. Then*

$$\mathrm{WF}(\mathcal{P}_1 \circ \mathcal{P}_2) \subset C_1 \circ C_2$$
$$\mathrm{WF}((\mathcal{P}_1 \circ \mathcal{P}_2)u) \subset (C_1 \circ C_2) \circ \mathrm{WF}(u).$$

From an imaging point of view the operator that is studied is the image reconstruction operator $\mathcal{P}^*\mathcal{P}$ where $\mathcal{P}^*$ is the adjoint of the FIO $\mathcal{P}$. Using Hörmander-Sato Lemma, one can study the wavefront set of the image reconstruction operator. For this we require the canonical relation [44] of the adjoint $\mathcal{P}^*$ which is given by

$$C^t = \{(y, \eta \mathrm{d}y; x, \xi \mathrm{d}x) : (x, \xi \mathrm{d}x; y, \eta \mathrm{d}y) \in C\}.$$

Now from Hörmander-Sato Lemma, we have,

$$\mathrm{WF}(\mathcal{P}^*\mathcal{P}) \subset C^t \circ C$$

so, when the composition is defined, $\mathrm{WF}(\mathcal{P}^*\mathcal{P}f) \subset (C^t \circ C) \circ \mathrm{WF}(f)$.

1.5 Applications to Tomography

In this section we apply what we've presented about wavefront sets to explain strengths and limitations of the reconstruction methods we presented in Section 1.2.

1.5.1 Microlocal Analysis in X-ray CT

In section 1.2.1, we saw reconstructions from different limited data problems had different strengths and weaknesses. To understand why, we use the information in the last chapter to understand the microlocal analysis of $\mathcal{R}_L$. To make the tangent coordinates simpler, we will use coordinates on $S^1 \times \mathbb{R}$ $(\varphi, p) \mapsto (\omega(\varphi), p)$ where we recall $\omega(\varphi) = (\cos(\varphi), \sin(\varphi))$ and $\omega^\perp(\varphi) = \omega(\varphi + \pi/2)$. Thus, functions on $S^1 \times \mathbb{R}$ will be written in terms of (φ, p).

Theorem 17. *The Radon transform $\mathcal{R}_L$ is an elliptic FIO associated to the canonical relation*

$$\begin{aligned} C_L = \{ &\big(\varphi, p, \alpha(-x\cdot\omega^{\perp}(\varphi)\mathrm{d}\varphi + \mathrm{d}p); x, \alpha\omega(\varphi)\mathrm{d}x\big) \\ &: (\varphi,p)\in[0,2\pi]\times\mathbb{R}, x\in\mathbb{R}^2, \alpha\neq 0, x\cdot\omega(\varphi)=p\} \end{aligned} \tag{1.51}$$

Furthermore, $C_L^t \circ C_L = \Delta$ is the diagonal in $\big(T^*(\mathbb{R}^2)\backslash\mathbf{0}\big)^2$.

Proof. In Example 10, we showed that $\mathcal{R}_L$ is a FIO associated to phase function

$$\phi(\varphi, p, x, \tau) = \tau(p - x\cdot\omega(\varphi)).$$

To calculate the canonical relation for $\mathcal{R}_L$, we follow the general methods outlined in Section 1.4.3 (see also [45, p. 165] or [92, (6.1) p. 462]). We first calculate the differentials of ϕ,

$$\begin{gathered} \partial_x\phi = -\tau\omega(\varphi)\mathrm{d}x, \quad \partial_{(\varphi,p)}\phi = \tau\left(-x\cdot\omega^{\perp}(\varphi)\mathrm{d}\varphi + \mathrm{d}p\right) \\ \partial_\tau\phi = (p - x\cdot\omega(\varphi))\mathrm{d}\tau. \end{gathered} \tag{1.52}$$

Note that the conditions for ϕ to be a nondegenerate phase function [92, (2.2)-(2.4), p. 315] hold because $\partial_x\phi$ and $\partial_{(\varphi,p)}\phi$ are not zero for $\tau\neq 0$. Therefore $\mathcal{R}_L$ is a Fourier integral operator. $\mathcal{R}_L$ has order $-1/2$ because its symbol $1/2\pi$ is homogeneous of degree zero, $2 = \dim\mathbb{R}^2 = \dim Y$, and σ is one dimensional (see [92, p. 462 under (6.3)]). Since the symbol, $1/2\pi$, is homogeneous and nowhere zero, $\mathcal{R}_L$ is elliptic (see [44]).

The auxiliary manifold Σ_ϕ is

$$\Sigma_\phi = \{(\varphi, p, x, \tau)\in([0,2\pi]\times\mathbb{R})\times\mathbb{R}^2\times(\mathbb{R}\backslash\mathbf{0}) : p - x\cdot\omega(\varphi) = 0\}. \tag{1.53}$$

The canonical relation, C_L associated to $\mathcal{R}_L$ is defined by the map

$$\Sigma_\phi \ni (x,\varphi,p,\tau)\mapsto \left(\varphi, (x\cdot\omega(\varphi)); \partial_{(\varphi,p)}\phi; x, -\partial_x\phi\right).$$

One uses this and a calculation to justify the expression (1.51).

To show $C_L^t\circ C_L = \Delta$ we let $(x,\xi\mathrm{d}x)\in T^*(\mathbb{R}^2)$ and follow it through the calculation of $C_L^t\circ C_L$ using (1.51). Choose $\varphi\in[0,2\pi]$ such that $\xi = a\omega(\varphi)$ for some $a>0$. Then, there are two vectors associated to $(x,\xi\mathrm{d}x)$ in C_L,

$$\begin{aligned} \lambda_1 &= \varphi, x\cdot\omega(\varphi); a(-x\cdot\omega^{\perp}(\varphi)\mathrm{d}\varphi, \mathrm{d}p)), \\ \lambda_2 &= (\varphi+\pi, x\cdot\omega(\varphi+\pi); -a(-x\cdot\omega^{\perp}(\varphi+\pi)\mathrm{d}\varphi + \mathrm{d}p). \end{aligned}$$

Under C_L^t, λ_1 is associated with $(x\cdot\omega(\varphi))\omega(\varphi) + x\cdot\omega^{\perp}(\varphi), a\omega(\varphi)\mathrm{d}x)$ and this is exactly $(x,\xi\mathrm{d}x)$, and there is no other vector in $T^*(\mathbb{R}^2)$ associated with λ_1 (i.e., $(x,\xi,\lambda_1)\in C_L^t$). In a similar way, one shows the only vector in $T^*(\mathbb{R}^2)$ associated with λ_2 is $(x,\xi\mathrm{d}x)$. Therefore

$$C_L^t\circ C_L = \left\{(x,\xi\mathrm{d}x; x,\xi\mathrm{d}x) : (x,\xi\mathrm{d}x)\in T^*(\mathbb{R}^2)\backslash\mathbf{0}\right\} = \Delta.$$

□

Note that the fact $C_L^t \circ C_L = \Delta$ implies that $\mathrm{WF}\left(\mathcal{R}_L^*\mathcal{R}_L(f)\right) \subset \mathrm{WF}(f)$, by the Hörmander-Sato Lemma (Theorem 16), and this and the theorem about composition of FIO [44, Theorem 4.2.2] provides another proof that $\mathcal{R}_L^*\mathcal{R}_L$ is a ΨDO.

This theorem has the following important corollaries.

Corollary 1 (Propagation of Singularities for $\mathcal{R}_L$). *Let $f \in \mathcal{E}'(\mathbb{R}^2)$.*

a. Let $(x_0, \xi_0 \mathrm{d}x) \in T^*(\mathbb{R}^2)\backslash\mathbf{0}$ and let φ_0 be chosen so that $\xi_0 = \alpha\omega(\varphi_0)$ for some $\alpha \neq 0$. If $(x_0, \xi_0 \mathrm{d}x) \in \mathrm{WF}(f)$, then $(\varphi_0, x_0 \cdot \omega(\varphi_0); \alpha(-x_0 \cdot \omega^\perp(\varphi_0)\mathrm{d}\varphi + \mathrm{d}p) \in \mathrm{WF}(\mathcal{R}_L f)$.

b. Let $(\varphi_0, p_0) \in [0, 2\pi] \times \mathbb{R}$ and assume $(\varphi_0, p_0; \alpha(-A\mathrm{d}\varphi + \mathrm{d}p)) \in \mathrm{WF}(\mathcal{R}_L f)$. Then, $(x_0, \xi_0 \mathrm{d}x) \in \mathrm{WF}(f)$ where $x_0 = p_0\omega(\varphi_0) + A\omega^\perp(\varphi_0)$ and $\xi_0 = \alpha\omega(\varphi_0)$.

This provides the paradigm:

$\mathcal{R}_L$ detects singularities of f perpendicular to the line of integration ("visible" directions) but not in other ("invisible") directions.

Remark 2. The paradigm has implications for limited data tomography. A wavefront direction $(x_0, \xi_0 \mathrm{d}x) \in \mathrm{WF}(f)$ will be visible from limited Radon data if and only if the line through x_0 perpendicular to ξ_0 is in the data set.

Proof. Because $\mathcal{R}_L$ is elliptic,

$$(x_0, \xi_0 \mathrm{d}x) \in \mathrm{WF}(f) \text{ if and only if } C_L \circ \{(x_0, \xi_0 \mathrm{d}x)\} \in \mathrm{WF}(\mathcal{R}_L f).$$

Here we use a stronger version of the Hörmander-Sato Lemma for elliptic operators [92]. Part a. follows from the $\Rightarrow$ implication of this equivalence and part b. follows from the $\Leftarrow$ implication using the expression for C_L, (1.51).

Part a. implies that $\mathcal{R}_L$ detects singularities perpendicular to the line being integrated over, since $\omega(\varphi_0)$ is perpendicular to the line $L(\omega(\varphi_0), x_0 \cdot \omega(\varphi_0))$, and Part b. implies that if a singularity is visible in $\mathcal{R}_L f$ at (φ_0, p_0), it must come from a point on $L(\omega(\varphi_0), p_0)$ and in a direction perpendicular to this line. This explains the paradigm in the theorem. □

Corollary 2 (Propagation of Singularities for Reconstruction Operators). *Let $f \in \mathcal{E}'(\mathbb{R}^2)$.*

a. Let $\mathcal{L}$ be either the FBP (see (1.18)), Lambda ($\mathcal{L}_x$, (1.22)), or Lambda + contour ($\mathcal{L}_{x,\mu}$, (1.23)) operators. Let $f \in \mathcal{E}'(\mathbb{R}^2)$. Then, $\mathrm{WF}(f) = \mathrm{WF}(\mathcal{L}f)$.

b. Let $\mathcal{R}_{L,\mathrm{lim}}$ be the limited angle backprojection operator in (1.25) for angles $a < \varphi < b$ (where $b - a < \pi$). Let $\mathcal{V} = \{(x, \xi \mathrm{d}x) : \xi = \alpha\omega(\varphi), \varphi \in (a, b)\}$. If $\mathcal{L}_{\mathrm{lim}}$ is any of the operators

$$\mathcal{R}_{L,\mathrm{lim}}\Lambda_p\mathcal{R}_L, \quad \mathcal{R}_{L,\mathrm{lim}}\left(-\frac{d^2}{dp^2}\mathcal{R}_L\right), \quad \mathcal{R}_{L,\mathrm{lim}}\left(\left(-\frac{d^2}{dp^2} + \mu\right)\mathcal{R}_L\right),$$

then

$$\mathrm{WF}(\mathcal{L}_{\mathrm{lim}} f) \cap \mathcal{V} = \mathrm{WF}(f) \cap \mathcal{V}\,.$$

Proof. Part a follows from the fact that both $\mathcal{L}_x$ and $\mathcal{L}_{x,\mu}$ are elliptic, as noted in Example 9 and the strong pseudolocal property in Theorem 14.

Part b follows from the fact that, when one cuts off angles, one can see only wavefront parallel the angles in the data set, that is, the visible directions in $\mathcal{V}$. A complete proof of this result is given in [24]. □

Remark 3. The paradigms in Corollaries 1 and 2 have especially simple interpretations if f is the sum of characteristic functions of sets with smooth boundaries. The tangent line to any point on the boundary of a region is normal to the wavefront direction of f at that point (since in the wavefront set at that point is normal the boundary, see Example 6).

So, a boundary at x (with conormal $(x, \xi \mathrm{d}x)$) will be visible from the data $\mathcal{R}_L f$ near $(\omega(\varphi), p)$ if (x, ξ) is normal to the line of integration (equivalently:. the boundary at x is tangent to a line in the data set).

Finally, note that Example 1 provided an simple case for which $\mathcal{R}_L f$ is not smooth when the line $L(\varphi, p)$ is tangent to the boundary of $\mathrm{supp}(f)$. The paradigm show this principle is true generally.

1.5.2 Limited data X-ray CT

Now we examine each of the limited data problems we discussed in Section 1.2 in light of the corollaries and paradigm of the last section.

Exterior X-ray CT data

In the reconstruction in Figure 1.2 the boundaries tangent to lines in the data set are clearer and less fuzzy than the one not tangent to lines in the data set. The paradigm in Corollary 1 and Remarks 2 and 3 explain this perfectly. When a line in the data set is tangent to a boundary, then the boundary is visible in the reconstruction. For our exterior reconstruction in Figure 1.2, this is true even for the inside boundary of the disk at about eight o'clock on the circle (lower left); that boundary is imaged by only a few lines in the exterior data set. If the line tangent to the boundary at x is not in the data set, then the boundary is fuzzier, as is true in that figure for the "invisible" boundaries.

This is reflected in Quinto's algorithm [74] in the following way. That algorithm expands the reconstruction in a polar Fourier series

$$f(r\omega(\varphi)) = \sum_{\ell \in \mathbb{Z}} f_\ell(r) e^{i\ell\varphi},$$

where $f_\ell(r)$ is approximated by a polynomial which is calculated using quadrature. The calculation of f_ℓ can be done stably only up to about $|\ell| = 25$ and so the reconstruction is not terribly good in polar direction. However, for each ℓ for which this can be done, the recovery of $f_\ell(r)$ is very accurate and can be done up to a polynomial of order about 100. Thus the algorithm has good

radial resolution but bad resolution in the polar direction. However, this is, at least in part, a limitation of the problem, not just the algorithm. The singularities in Figure 1.2 that are smoothed by the algorithm are intrinsically difficult to reconstruct.

Limited Angle Data

In Figure 1.3, data are given over lines $L(\omega(\varphi), p)$ for $\varphi \in [-\pi/4, \pi/4]$ and the only boundaries that are visible are exactly those normal to such lines. This reflects Corollary 1 and Remarks 2 and 3. The algorithm used is FBP but with a limited angle backprojection (see (1.25), in that reconstruction only between $a = -\pi/4$ and $b = \pi/4$, which was described in Section 1.3.5, below 1.25. In this case, Corollary 2 shows that the only singularities of f that will be visible in $\mathcal{L}_{\text{lim}} f$ (where $\mathcal{L}_{\text{lim}}$ is given in that corollary) are those in the cone $\{r\omega(\varphi) : \varphi \in (-\pi/4, \pi/4), r \neq 0\}$.

However, there is also a marked streak along the lines with angle $\varphi = \pm\pi/4$ that are tangent to the boundary of the region. Frikel and Quinto have recently explained it using microlocal analysis [24]. They also explained why, to decrease those streaks, one needs to make the backprojection operator a standard FIO by including a smooth cutoff function ψ supported in $[-\pi/4, \pi/4]$ that is equal to 1 on most of that interval.

$$\mathcal{R}_L^*{}_\psi g(x) = \int_{\varphi=-\pi/4}^{\pi/4} g(\omega(\varphi), x \cdot \omega(\varphi))\psi(\varphi)\mathrm{d}\varphi\,.$$

Region of Interest (ROI) Data

The reconstruction in Figure 1.4 is from Lambda CT and all singularities of the circle are visible. This is true because $\mathcal{R}_L^*\mathcal{R}_L$ is an elliptic pseudodifferential operator as is

$$\mathcal{L}_x = (-\Delta)\,\mathcal{R}_L^*\mathcal{R}_L$$

as explained in Example 9. Therefore, $\mathrm{WF}(\mathcal{L}_x(f)) = \mathrm{WF}(f)$ for any distribution f of compact support. Recall that $\mathcal{L}_x(f)(x)$ determined by data $\mathcal{R}_L f$ for lines near x. This means that the wavefront of f above x is the same as the wavefront set of $\mathcal{L}_x(f)$ above x, which can be determined by local data for lines near x. This is why all singularities are visible in the Lambda reconstruction in that figure.

This also means that any null function for the interior problem must be smooth in the ROI since its Radon data are zero (e.g., smooth) for lines meeting the ROI.

1.5.3 Microlocal Analysis of conical tilt Electron Microscope Tomography (ET)

We will use the notation of Section 1.3.7. We let

$$S_\alpha = \{(\sin(\alpha)\cos(\varphi), \sin(\alpha)\sin(\varphi), \cos(\alpha)) \,:\, \varphi \in [0, 2\pi]\}$$
$$C_\alpha = \mathbb{R}S_\alpha \,.$$

In Theorem 10, we showed that the operators $\mathcal{L}_\Delta$ (see (1.28)) and $\mathcal{L}_S$ (see (1.29)) can be expressed using the convolution

$$f * I(x) = \int_{y \in C_\alpha} f(x+y) \frac{1}{\|y\|} \mathrm{d}y$$

where $\mathrm{d}y$ is the surface area measure on the cone C_α. In particular we proved

$$\begin{aligned} \mathcal{P}_S^* \mathcal{P}_S f &= f * I \\ \mathcal{L}_\Delta f &= (-\Delta)\,(f * I) \\ \mathcal{L}_S f &= \left(-\Delta + \csc^2(\alpha) \frac{\partial^2}{\partial z^3}\right) f * I \,. \end{aligned}$$

As one can see from the cross-section in the $x-y$-plane of the reconstruction, Figure 1.5, there are circular artifacts. In the cross-section in the vertical plane $x = -y$, Figure 1.6, there are streak artifacts coming off each of the balls at a 45° angle.

These artifacts can be understood intuitively. Let f be the characteristic function of a ball B. Then, $f * I(x)$ integrates f over the cone $x + C_{\pi/4}$. When this cone is tangent to B at a point besides x, it is normal to a singularity of f at this point. We claim that this singularity will cause a singularity of $f * I$ at x. The reason is, when x is perturbed, the cone moves in and out of B, so the integral changes from 0 (when the cone is disjoint from B) to nonzero values as the cone intersects B. A calculation will convince one that the singularity is a discontinuity in the first derivative. Because $\mathcal{L}_\Delta$ is a derivative of $f * I$, that singularity is accentuated in $\mathcal{L}_\Delta f$ at x. One can see this phenomenon from the artifacts in $\mathcal{L}_\Delta$ reconstructions in Section 1.2.2. In the $x-y$-plane, the artifacts are circular shadows from the disks outside of the plane; in the $y = -x$ plane, the artifacts follow along the generating lines of the cone. However, this is not a rigorous explanation since it does not apply to arbitrary functions. It also does not explain why the $\mathcal{L}_\Delta$ reconstruction has apparent singularities but the $\mathcal{L}_S$ reconstruction seems not to.

Our next theorem explains this using microlocal analysis. To state the theorem, we recall the definition of conormal bundle of a submanifold $B \subset \mathbb{R}^3$ as

$$N^*(B) = \{(y, \xi \mathrm{d}x) \,:\, y \in B, \xi \text{ is normal to } B \text{ at } y\} \,.$$

Theorem 18 ([21]). *The conical Tilt ET operator $\mathcal{P}_S$ is an elliptic Fourier integral operator. Let $f \in \mathcal{E}'(\mathbb{R}^3)$ and let $\alpha \in (0, \pi/2)$. Let $\mathcal{L}$ be either $\mathcal{L}_\Delta$ or $\mathcal{L}_S$. Then,*

$$\mathrm{WF}(\mathcal{L}(f)) \subset (\mathrm{WF}(f) \cap \mathcal{V}) \cup \mathcal{A}(f)$$

where

$$\mathcal{V} = \mathbb{R}^3 \times \left\{\eta \in \mathbb{R}^3 \backslash \mathbf{0} \,:\, \exists \omega \in S_\alpha,\ \eta \cdot \omega = 0\right\}$$

represents the set of possible visible singularities and the added artifacts come from

$$\mathcal{A}(f) = \{(x, \xi \mathrm{d}x) \,:\, \exists\, (y, \xi \mathrm{d}x) \in N^*(x + C_\alpha) \cap \mathrm{WF}(f)\}\ .$$

Furthermore, the added artifacts in $\mathcal{A}(f)$ are stronger in Sobolev scale in $\mathcal{L}_\Delta f$ than in $\mathcal{L}_S f$.

Here $\mathcal{V}$ is the set of visible singularities, those from f that should appear in $\mathcal{L}f$. The set $\mathcal{A}(f)$ consists of added artifacts, those caused by wavefront of f normal to $x + C_\alpha$ at points besides x. In Figure 1.5, the added artifacts in the $\mathcal{L}_\Delta$ reconstruction are exactly those that come from cones $x + C_\alpha$ that are tangent to boundaries of disks in $\mathrm{supp}(f)$, and this gives the same conclusions as the heuristic description given above Theorem 18.

The final statement in the theorem follows from the fact that $\mathcal{L}_\Delta$ is a class of singular FIO (so called $I^{p,l}$ classes) and $\mathcal{L}_S$ is in a better behaved class. These classes of singular FIOs will be discussed at the end of the next section.

The set of visible singularities $\mathcal{V}$ is larger for conical tilt ET than for the standard data acquisition geometry, single axis tilt ET and this is one reason to use it, even though acquiring data can be more difficult.

The proof of this theorem uses the Hörmander-Sato Lemma (Theorem 16). One first calculates the canonical relation, C, and then one calculates $C^t \circ C$ and shows $C^t \circ C$ has two parts, One is $\mathcal{V}$, the set of visible singularities, singularities of f that will be visible in $\mathcal{L}_\Delta f$. The second part generates the set of added artifacts, $\mathcal{A}(f)$. Then, deep results in [29] are used to explain why $\mathcal{L}_S$ is better than $\mathcal{L}_\Delta$.

This conical tilt transform is a so called admissible Radon transform [25]. The microlocal analysis of admissibility was first studied in [33]. A thorough, deep analysis of the microlocal properties of these transforms in a very general setting is given in [28] including general results for backprojection that are related to Theorem 18.

Quinto and Rullgård have proven similar results for a curvilinear Radon transform for which the more effective differential operator (analogous to $\mathcal{D}_S$) decreases the strength of artifacts only locally [78].

1.5.4 SAR Imaging

In this section, we will describe some recent results on SAR imaging. The results described here emphasize a microlocal analysis point of view. The notation we follow is from Section 1.2.3. We recall that the forward operator under consideration is

$$\mathcal{P}V(s,t) = \int e^{-\mathrm{i}\omega(t - (\|x - \gamma_T(s)\| + \|x - \gamma_R(s)\|)/c_0)} A(s,t,x,\omega) V(x) \mathrm{d}x \mathrm{d}\omega. \quad (1.54)$$

The canonical relation wherever it is well-defined is given by

$$C = \Bigg\{ s, t, -\omega \Bigg(\left(\frac{x-\gamma_T(s)}{\|x-\gamma_T(s)\|} \cdot \gamma_T'(s) + \frac{x-\gamma_R(s)}{\|x-\gamma_R(s)\|} \cdot \gamma_R'(s) \right) \mathrm{d}s + \mathrm{d}t \Bigg); \\ x_1, x_2, -\omega \left(\frac{x-\gamma_T(s)}{\|x-\gamma_T(s)\|} + \frac{x-\gamma_R(s)}{\|x-\gamma_R(s)\|} \right) \mathrm{d}x \\ : c_0 t = \|x-\gamma_T(s)\| + \|x-\gamma_R(s)\|, \omega \neq 0 \Bigg\}. \tag{1.55}$$

Note that (s, x, ω) is a global parametrization for C. Let us denote

$$Y = \{(s,t) \in (0,\infty) \times (0,\infty)\}$$

and $\{x_1, x_2\}$ space as X. One is interested in studying the imaging operator $\mathcal{F}^*\mathcal{P}$. Standard composition calculus of FIOs, the so-called transverse intersection calculus of Hörmander and the clean intersection calculus of Duistermaat and Guillemin, and Weinstein do not apply in general in these situations. Therefore one approach to understanding the imaging operator is to study the canonical left and right projections from the canonical relation $C \subset T^*Y \times T^*X$ to T^*Y and T^*X respectively.

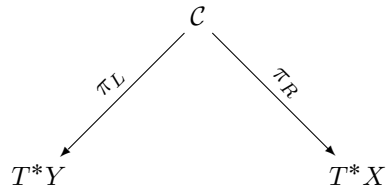

(1.56)

In order to motivate the results that follow, let us consider the following example.

Example 12. Let us consider a simple example from SAR imaging . This example will help us explain via microlocal analysis, some of the artifacts introduced by image reconstruction operator in 1.7.

Assume that a colocated transmitter/receiver traverses the straight trajectory $\gamma(s) = (s, 0, h)$ with h fixed. The forward operator in this case is

$$\mathcal{P}f(s,t) = \int e^{-\mathrm{i}\omega\left(t - \frac{2}{c_0}\sqrt{(x-s)^2+y^2+h^2}\right)} A(s,t,x,y,\omega) f(x,y) \mathrm{d}x \mathrm{d}y \mathrm{d}\omega.$$

The canonical relation of this operator is easily computed to be

$$C = \Bigg\{ s, \frac{2}{c_0}\sqrt{(x-s)^2+y^2+h^2}, -\omega \left(\frac{2}{c_0} \frac{x-s}{\sqrt{(x-s)^2+y^2+h^2}} \mathrm{d}s + \mathrm{d}t \right); \\ x, y, -\frac{2\omega}{c_0} \left(\frac{x-s}{\sqrt{(x-s)^2+y^2+h^2}} \mathrm{d}x + \frac{y}{\sqrt{(x-s)^2+y^2+h^2}} \mathrm{d}y \right) \Bigg\}.$$

Now using Hörmander-Sato Lemma, we have,

$$\mathrm{WF}(\mathcal{P}^*\mathcal{P}) \subset \Bigg\{ x, y, \frac{2\omega}{c_0}\left(\frac{x-s}{\sqrt{(x-s)^2+y^2+h^2}}\mathrm{d}x + \frac{y}{\sqrt{(x-s)^2+y^2+h^2}}\mathrm{d}y\right);$$
$$z, w, \frac{2\omega}{c_0}\left(\frac{z-s}{\sqrt{(z-s)^2+w^2+h^2}}\mathrm{d}z + \frac{w}{\sqrt{(z-s)^2+w^2+h^2}}\mathrm{d}w\right) :$$
$$\sqrt{(x-s)^2+y^2+h^2} = \sqrt{(z-s)^2+w^2+h^2} \text{ and}$$
$$\frac{x-s}{\sqrt{(x-s)^2+y^2+h^2}} = \frac{z-s}{\sqrt{(z-s)^2+w^2+h^2}}, \omega \neq 0 \Bigg\}.$$

We then have that $(z, w) = (x, y)$ or $(z, w) = (x, -y)$. The first equality contributes to the diagonal relation of the wavefront set of $\mathcal{P}^*\mathcal{P}$ while the second contributes to the relation formed by reflection about the x-axis. In other words, we have that

$$\mathrm{WF}(\mathcal{P}^*\mathcal{P}) \subset \triangle \cup G, \text{ where } \triangle = \{(x, y, \xi \mathrm{d}x + \eta \mathrm{d}y : x, y, \xi \mathrm{d}x + \eta \mathrm{d}y)\}$$
$$\text{and } G = \{(x, y, \xi \mathrm{d}x + \eta \mathrm{d}y; x, -y, \xi \mathrm{d}x - \eta \mathrm{d}y)\}.$$

The presence of the set G as in the above example (the non-diagonal part) indicates that the imaging operator introduces artifacts in the reconstructed image. A detailed study of the class of distributions as in the example above, called $I^{p,l}$ classes, was introduced in [63, 36, 30, 29]. These class of distributions have come up in the study of several imaging problems [28, 30, 29, 43, 67, 19, 20, 21, 22, 53, 1]. In instances where the imaging operator introduces artifacts, it is of interest to determine whether the artifacts are of the same strength in a suitable sense as that of the true singularities and whether the artifacts can be suppressed or displaced from the true singularities. These questions are answered in the references mentioned in the previous paragraph.

Monostatic SAR imaging

In monostatic SAR imaging, the transmitter and receiver are located at the same point. In other words, $\gamma_T(s) = \gamma_R(s)$. Nolan and Cheney in [68] investigated the microlocal properties of the forward operator $\mathcal{P}$ and the associated image reconstruction operator $\mathcal{P}^*\mathcal{P}$. Using microlocal tools, synthetic aperture inversion in the presence of noise and clutter was done in [96]. This operator was further investigated by Felea in [17] and she made a detailed analysis of the image reconstruction operator for various flight trajectories. Felea in [17] showed that for $\gamma(s) = (s, 0, h)$ with $h > 0$ fixed, the operator $\mathcal{P}^*\mathcal{P}$ belongs to $I^{2m,0}(\Delta, G)$ where $\Delta = \{(x, \xi, x, \xi)\} \in T^*X \times T^*\backslash\{0\}$ and G is the graph of the function $\chi(x_1, x_2, \xi_1, \xi_2) = (x_1, -x_2, \xi_1, -\xi_2)$. If $\gamma(s) = (\cos s, \sin s, h)$, it was shown in [18] that $\mathcal{P}^*\mathcal{P} \in I^{2m,0}(\Delta, G)$, where G is a 2-sided fold. For mappings with singularities (such as folds and blowdowns) we refer to [27, 34]. Furthermore, in [18], Felea showed that in some

instances such as the flight trajectory being circular, the artifact singularities of the same strength as the true singularities can be displaced far away from the true singularities and those that are not displaced are of lesser strength compared to the true singularities. In [88], the authors show that cancellation of singularities, that is only certain singularities are recoverable, can occur even in curved flight paths.

Bistatic SAR imaging

We now discuss some recent results by the authors and their collaborators investigating the microlocal properties of transforms that appear in bistatic SAR imaging. For related work, we refer the reader to [95].

Common offset bistatic SAR imaging

In common offset SAR imaging, the transmitter and receiver travel in a straight line offset by a constant distance at all times. More precisely, let

$$\gamma_T(s) = (s + \alpha, 0, h) \text{ and } \gamma_R(s) = (s - \alpha, 0, h)$$

be the trajectories of the transmitter and receiver respectively with α and h fixed positive quantities. A detailed microlocal analysis of associated forward operator $\mathcal{P}$ and the imaging operator $\mathcal{P}^*\mathcal{P}$ was done in [53]. The authors obtained the following results analogous to the ones obtained by Nolan and Cheney in [68] and Raluca Felea in [17].

Theorem 19 ([53]). *Let $\gamma_T(s) = (s+\alpha, 0, h)$ and $\gamma_R(s) = (s-\alpha, 0, h)$ where $\alpha > 0, h > 0$ are fixed. The operator $\mathcal{P}$ defined in* (1.54) *is an FIO. The canonical relation C associated to $\mathcal{P}$ defined in* (1.55) *satisfies the following: The projections π_L and π_R defined in* (1.56) *are a fold and blowdown respectively.*

Theorem 20 ([53]). *Let $\mathcal{P}$ be defined with γ_T and γ_R given in Theorem 19. Then $\mathcal{P}^*\mathcal{P} \in I^{3,0}(\Delta, G)$, where Δ is the diagonal relation and G is the graph of the map $\chi(x_1, x_2, \xi_1, \xi_2) = (x_1, -x_2, \xi_1, -\xi_2)$.*

Common midpoint SAR imaging

In common midpoint SAR imaging, the transmitter and receiver travel in a straight line at a constant height above the ground at equal speeds away from a common midpoint. The trajectories of the transmitter and receiver for the common midpoint geometry we consider are

$$\gamma_t(s) = (s, 0, h) \text{ and } \gamma_r(s) = (-s, 0, h). \tag{1.57}$$

A detailed microlocal analysis of the forward operator (1.55) associated to γ_t and γ_r and the imaging operator $\mathcal{P}^*\mathcal{P}$ was done in [1]. In contrast to the

results in [68, 17, 53], here the canonical relation C associated to $\mathcal{P}$ is a 4-1 relation and this is reflected in the fact the canonical left and right projections π_L and π_R drop rank on a union of two disjoint sets. More precisely, we obtain the following results for the forward operator and the imaging operator, respectively.

Theorem 21 ([1]). *Let $\mathcal{P}$ be as in* (1.54) *with the trajectories given by* (1.57). *Then $\mathcal{P}$ is an FIO and the canonical relation associated to $\mathcal{P}$ defined in* (1.55) *has global parametrization*

$$(0,\infty)\times\left(\mathbb{R}^2\backslash 0\right)\times(\mathbb{R}\backslash 0)\ni(s,x_1,x_2,\omega)\mapsto C,$$

and it satisfies the following: the left and right projections π_L and π_R drop rank simply by one on a set $\Sigma=\Sigma_1\cup\Sigma_2$ where in the coordinates (s,x,ω), $\Sigma_1=\{(s,x_1,0,\omega)\,:\,s>0,|x_1|>\epsilon',\omega\neq 0\}$ and $\Sigma_2=\{(s,0,x_2,\omega)\,:\,s>0,|x_2|>\epsilon',\omega\neq 0\}$ for $0<\epsilon'$ small enough. The canonical relation C associated to $\mathcal{P}$ satisfies the following: The projections π_L and π_R defined in (1.56) *are a fold and blowdown respectively along Σ.*

Theorem 22 ([1]). *Let $\mathcal{P}$ be as in* (1.54) *with the trajectories given by* (1.57). *Then $\mathcal{P}^*\mathcal{P}$ can be decomposed into a sum belonging to $I^{2m,0}(\Delta,G_1)+I^{2m,0}(\Delta,G_2)+I^{2m,0}(G_1,G_3)+I^{2m,0}(G_2,G_3)$, where G_i for $i=1,2,3$ are the graphs of the following functions χ_i for $i=1,2,3$ on T^*X:*

$$\chi_1(x,\xi)=(x_1,-x_2,\xi_1,-\xi_2),\chi_2(x,\xi)=(-x_1,x_2,-\xi_1,\xi_2)\text{ and }\chi_3=\chi_1\circ\chi_2.$$

1.5.5 Summary

Finally, we would like to point out some important themes of this chapter.

Microlocal analysis can help understand strengths and limitations of tomographic reconstruction methods. For limited data X-ray tomography, we used microlocal analysis to show shows which singularities of functions will be visible depending on the data, and our reconstructions illustrated the paradigm.

Each of the reconstruction methods we described is of the form

$$\mathcal{L}=\mathcal{P}^*\mathcal{D}\mathcal{P}$$

where the forward operator (operator modeling the tomography problem) $\mathcal{P}$ is a Fourier integral operator and $\mathcal{P}^*$ is an adjoint and $\mathcal{D}$ is a pseudodifferential operator. In SAR imaging, $\mathcal{D}=\mathrm{Id}$ is the identity operator and the reconstruction method is $\mathcal{P}^*\mathcal{P}$–the normal operator. Since the operator $\mathcal{D}$ is a differential or pseudodifferential operator, it does not add to the wavefront set of $\mathcal{P}f$, $\mathrm{WF}(\mathcal{D}\mathcal{P}f)\subset\mathrm{WF}(\mathcal{P}f)$. If $\mathcal{D}$ is elliptic (on the range of $\mathcal{P}$, which is true in the cases we consider), $\mathrm{WF}(\mathcal{D}\mathcal{P}f)=\mathrm{WF}(\mathcal{P}f)$. Then, one needs to understand what $\mathcal{P}^*$ does, and this is determined by the structure of $C^t\circ C$ by the Hörmander Sato Lemma (Theorem 16):

$$\mathrm{WF}\left(\mathcal{P}^*\left(\mathcal{D}\mathcal{P}f\right)\right) \subset \left(C^t \circ C\right) \circ \mathrm{WF}(f)\,.$$

However, in limited angle tomography, because $\mathcal{R}_{L,\mathrm{lim}}$ is not a standard FIO, $\mathcal{R}_{L,\mathrm{lim}}\mathcal{D}\mathcal{R}_L$ adds singularities along lines at the ends of the limited angular range.

In the case of SAR and conical tilt ET, $C^t \circ C$ is more complicated; it includes Δ and another set. In conical tilt ET, this extra set generates the set $\mathcal{A}(f)$ of extra artifacts given in Theorem 18. Also, for conical tilt ET, we noted that a well-chosen differential operator ($(-\mathcal{D}_S)$ rather than $(-\Delta_S)$) decreases the strength of the added singularities: they are visible if one looks carefully at the reconstructions, but they are smoother than when $(-\Delta_S)$ is used.

The only exact reconstruction method we presented is FBP (Theorem 9). The other algorithms, such as Lambda CT, involve differential operators and backprojection. We demonstrated, using microlocal analysis, that they do recover many (or all) singularities of the object.

Recovering singularities does not recover the object. So, these algorithms are not useful when one needs density values, such as in distinguishing tumor cells from benign cells in diagnostic radiology. However, in many cases, one is interested in the shapes of regions, not actual density values, so knowing the location of singularities is useful. The algorithm must be designed so that it clearly shows singularities in the reconstruction. For example, an algorithm that turns jump discontinuities in the object into discontinuities of a derivative in the reconstruction might not provide a clear picture of the object. Lambda CT and our algorithms for conical tilt ET actually accentuate singularities; they make the singularities more apparent since they are operators of order one (like a first derivative). The implementation smooths out the derivative since it uses numerical differentiation.

In conical tilt ET and SAR the reconstruction methods, that included a backprojection (adjoint, $\mathcal{P}^*$) produced added artifacts (as shown in Figures 1.6 and 1.7), and we explained them using microlocal analysis.

Microlocal analysis will not make a bad algorithm good, but it can show that some limitations in reconstruction quality are intrinsic to the underlying tomographic problem. It can point to where reconstruction methods need to be regularized more strongly because of intrinsic instability in the specific tomography problem. In summary, microlocal analysis can be used to understand practical and theoretical issues in tomography.

Acknowledgements

Both authors thank the American Institute of Mathematics and their colleagues Gaik Ambartsoumian, Raluca Felea, and Clifford Nolan in an AIM

SQuaREs for a better understanding of the microlocal analysis of radar imaging. They appreciate Jürgen Frikel's careful reading of the chapter. The second author thanks Jan Boman, Alfred Louis, Frank Natterer, and many other friends and colleagues for important discussions about tomography and microlocal analysis over the years.

The first named author was partially supported by NSF grant DMS 1109417 and the second named author was partially supported by NSF grant DMS 1311558.

References

[1] Ambartsoumian G, Felea R, Krishnan VP, Nolan C, Quinto ET (2013) A class of singular Fourier integral operators in synthetic aperture radar imaging. J Funct Anal 264(1):246–269, DOI 10.1016/j.jfa.2012.10.008, URL http://dx.doi.org/10.1016/j.jfa.2012.10.008

[2] Anastasio MA, Zou Y, Sidky EY, Pan X (2007) Local cone-beam tomography image reconstruction on chords. Journal of the Optical Society of America A 24:1569–1579

[3] Bates R, Lewitt R (1978) Image reconstruction from projections: I: General theoretical considerations, II: Projection completion methods (theory), III: Projection completion methods (computational examples). Optik 50:I: 19–33, II: 189–204, III: 269–278

[4] Bidwell S (2012) Limited angle tomography and microlocal analysis. Tech. rep., Tufts University, senior Honors Thesis with Highest Thesis Honors

[5] Boman J (1991) Helgason's support theorem for Radon transforms - a new proof and a generalization, Lecture Notes in Mathematics, vol 1497, Springer Verlag, Berlin, New York, pp 1–5

[6] Boman J, Quinto ET (1987) Support theorems for real analytic Radon transforms. Duke Math J 55:943–948

[7] Cheney M, Borden B (2009) Fundamentals of radar imaging, CBMS-NSF Regional Conference Series in Applied Mathematics, vol 79. Society for Industrial and Applied Mathematics (SIAM), Philadelphia, PA, DOI 10.1137/1.9780898719291, URL http://dx.doi.org/10.1137/1.9780898719291

[8] Cheney M, Borden B (2009) Problems in synthetic-aperture radar imaging. Inverse Problems 25(12):123,005, 18, DOI 10.1088/0266-5611/25/12/123005, URL http://dx.doi.org/10.1088/0266-5611/25/12/123005

[9] Cheney M, Bordon B (2014) Synthetic Aperture Radar Imaging. In: Scherzer O (ed) The Handbook of Mathematical Methods in Imaging, 2nd edn, Springer Verlag, New York

[10] Cormack AM (1963) Representation of a function by its line integrals with some radiological applications. J Appl Physics 34:2722–2727

[11] Cormack AM (1964) Representation of a function by its line integrals with some radiological applications II. J Appl Physics 35:2908–2913
[12] Davison M, Grünbaum F (1981) Tomographic Reconstruction with Arbitrary Directions. Comm Pure Appl Math 34:77–120
[13] Faridani A (2006) Tomography and Sampling Theory. In: The Radon Transform and Applications to Inverse Problems, American Mathematical Society, Providence, RI, USA, AMS Proceedings of Symposia in Applied Mathematics
[14] Faridani A, Ritman EL (2000) High-resolution computed tomography from efficient sampling. Inverse Problems 16:635–650
[15] Faridani A, Ritman EL, Smith KT (1992) Local tomography. SIAM J Appl Math 52(2):459–484, DOI 10.1137/0152026, URL http://dx.doi.org/10.1137/0152026
[16] Faridani A, Finch D, Ritman E, Smith KT (1997) Local tomography, II. SIAM J Appl Math 57:1095–1127
[17] Felea R (2005) Composition of Fourier integral operators with fold and blowdown singularities. Comm Partial Differential Equations 30(10-12):1717–1740, DOI 10.1080/03605300500299968, URL http://dx.doi.org/10.1080/03605300500299968
[18] Felea R (2007) Displacement of artefacts in inverse scattering. Inverse Problems 23(4):1519–1531, DOI 10.1088/0266-5611/23/4/009, URL http://dx.doi.org/10.1088/0266-5611/23/4/009
[19] Felea R, Greenleaf A (2008) An FIO calculus for marine seismic imaging: folds and cross caps. Comm Partial Differential Equations 33(1-3):45–77, DOI 10.1080/03605300701318716, URL http://dx.doi.org/10.1080/03605300701318716
[20] Felea R, Greenleaf A (2010) Fourier integral operators with open umbrellas and seismic inversion for cusp caustics. Math Res Lett 17(5):867–886, DOI 10.4310/MRL.2010.v17.n5.a6, URL http://dx.doi.org/10.4310/MRL.2010.v17.n5.a6
[21] Felea R, Quinto ET (2011) The microlocal properties of the local 3-D spect operator. SIAM J Math Anal 43(3):659–674
[22] Felea R, Greenleaf A, Pramanik M (2012) An FIO calculus for marine seismic imaging, II: Sobolev estimates. Math Ann 352(2):293–337, DOI 10.1007/s00208-011-0644-5, URL http://dx.doi.org/10.1007/s00208-011-0644-5
[23] Finch DV, Lan IR, Uhlmann G (2003) Microlocal Analysis of the Restricted X-ray Transform with Sources on a Curve. In: Uhlmann G (ed) Inside Out, Inverse Problems and Applications, Cambridge University Press, MSRI Publications, vol 47, pp 193–218
[24] Frikel J, Quinto ET (2013) Characterization and reduction of artifacts in limited angle tomography. Inverse Problems 29:125,007
[25] Gelfand IM, Graev MI (1961) Integral transformations connected with straight line complexes in a complex affine space. Soviet Math Doklady 2:809–812

[26] Gelfand IM, Graev MI, Vilenkin NY (1966) Generalized Functions, vol 5. Academic Press, New York
[27] Golubitsky M, Guillemin V (1973) Stable mappings and their singularities. Springer-Verlag, New York, graduate Texts in Mathematics, Vol. 14
[28] Greenleaf A, Uhlmann G (1989) Non-local inversion formulas for the X-ray transform. Duke Math J 58:205–240
[29] Greenleaf A, Uhlmann G (1990) Composition of some singular Fourier integral operators and estimates for restricted X-ray transforms. Ann Inst Fourier (Grenoble) 40(2):443–466, URL http://www.numdam.org/item?id=AIF_1990__40_2_443_0
[30] Greenleaf A, Uhlmann G (1990) Estimates for singular Radon transforms and pseudodifferential operators with singular symbols. J Funct Anal 89(1):202–232, DOI 10.1016/0022-1236(90)90011-9, URL http://dx.doi.org/10.1016/0022-1236(90)90011-9
[31] Grigis A, Sjöstrand J (1994) Microlocal analysis for differential operators, London Mathematical Society Lecture Note Series, vol 196. Cambridge University Press, Cambridge, an introduction
[32] Guillemin V (1975) Some remarks on integral geometry. Tech. rep., MIT
[33] Guillemin V (1985) On some results of Gelfand in integral geometry. Proceedings Symposia Pure Math 43:149–155
[34] Guillemin V (1989) Cosmology in $(2+1)$-dimensions, cyclic models, and deformations of $M_{2,1}$, Annals of Mathematics Studies, vol 121. Princeton University Press, Princeton, NJ
[35] Guillemin V, Sternberg S (1977) Geometric asymptotics. American Mathematical Society, Providence, R.I., mathematical Surveys, No. 14
[36] Guillemin V, Uhlmann G (1981) Oscillatory integrals with singular symbols. Duke Math J 48(1):251–267, URL http://projecteuclid.org/getRecord?id=euclid.dmj/1077314493
[37] Hahn MG, Quinto ET (1985) Distances between measures from 1-dimensional projections as implied by continuity of the inverse Radon transform. Zeitschrift Wahrscheinlichkeit 70:361–380
[38] Helgason S (1965) The Radon transform on Euclidean spaces, compact two-point homogeneous spaces and Grassman manifolds. Acta Math 113:153–180
[39] Helgason S (1980) Support of Radon transforms. Advances in Math 38:91–100
[40] Helgason S (2011) Integral geometry and Radon transforms. Springer, New York, DOI 10.1007/978-1-4419-6055-9, URL http://dx.doi.org.ezproxy.library.tufts.edu/10.1007/978-1-4419-6055-9
[41] Herman G (2014) Tomography. In: Scherzer O (ed) The Handbook of Mathematical Methods in Imaging, 2nd edn, Springer Verlag, New York
[42] Hertle A (1983) Continuity of the Radon transform and its inverse on Euclidean space. Mathematische Zeitschrift 184:165–192

[43] de Hoop MV (2003) Microlocal analysis of seismic inverse scattering. In: Inside out: inverse problems and applications, Math. Sci. Res. Inst. Publ., vol 47, Cambridge Univ. Press, Cambridge, pp 219–296
[44] Hörmander L (1971) Fourier Integral Operators, I. Acta Mathematica 127:79–183
[45] Hörmander L (2003) The analysis of linear partial differential operators. I. Classics in Mathematics, Springer-Verlag, Berlin, distribution theory and Fourier analysis, Reprint of the second (1990) edition [Springer, Berlin; MR1065993 (91m:35001a)]
[46] HY (2002) Bistatic synthetic aperture radar
[47] K N, S S, V K (2007) Bayesian multiresolution method for local tomography in dental X-ray imaging. Physics in Medicine and Biology 52:6663–6678
[48] Katsevich A (2006) Improved Cone Beam Local Tomography. Inverse Problems 22:627–643
[49] Katsevich A, Ramm A (1996) The Radon Transform and Local Tomography. CRC Press
[50] Katsevich AI (1997) Local tomography for the limited-angle problem. J Math Anal Appl 213:160–182
[51] Katsevich AI (2004) An improved exact filtered backprojection algorithm for spiral computed tomography. Adv in Appl Math 32:681–697
[52] Krishnan VP (2009) A support theorem for the geodesic ray transform on functions. J Fourier Anal Appl 15(4):515–520, DOI 10.1007/s00041-009-9061-5, URL `http://dx.doi.org.ezproxy.library.tufts.edu/10.1007/s00041-009-9061-5`
[53] Krishnan VP, Quinto ET (2011) Microlocal aspects of common offset synthetic aperture radar imaging. Inverse Probl Imaging 5(3):659–674, DOI 10.3934/ipi.2011.5.659, URL `http://dx.doi.org/10.3934/ipi.2011.5.659`
[54] Krishnan VP, Levinson H, Quinto ET (2012) Microlocal Analysis of Elliptical Radon Transforms with Foci on a Line. In: Sabadini I, Struppa DC (eds) The Mathematical Legacy of Leon Ehrenpreis, Springer Verlag, Berlin, New York, Springer Proceedings in Mathematics, vol 16, pp 163–182
[55] Kuchment P, Lancaster K, Mogilevskaya L (1995) On local tomography. Inverse Problems 11:571–589
[56] Kurusa Á (1994) Support theorems for totally geodesic Radon transforms on constant curvature spaces. Proc Amer Math Soc 122(2):429–435
[57] Lissianoi S (1994) On stability estimates in the exterior problem for the Radon transform. In: Quinto E, Ehrenpreis L, Faridani A, Gonzalez F, Grinberg E (eds) Tomography, impedance imaging, and integral geometry (South Hadley, MA, 1993), Lectures in Appl. Math., vol 30, Amer. Math. Soc., Providence, RI, pp 143–147

[58] Louis AK (1981) Analytische Methoden in der Computer Tomographie. Universität Münster, habilitationsschrift
[59] Louis AK (1981) Ghosts in tomography, the null space of the Radon transform. Mathematical Methods in the Applied Sciences 3:1–10
[60] Louis AK (1986) Incomplete data problems in X-ray computerized tomography I. Singular value decomposition of the limited angle transform. Numerische Mathematik 48:251–262
[61] Louis AK, Maaß P (1993) Contour reconstruction in 3-D X-Ray CT. IEEE Trans Medical Imaging 12(4):764–769
[62] Louis AK, Rieder A (1986) Incomplete data problems in X-ray computerized tomography II. Truncated projections and region-of-interest tomography. Numerische Mathematik 56:371–383
[63] Melrose RB, Uhlmann GA (1979) Lagrangian intersection and the Cauchy problem. Comm Pure Appl Math 32(4):483–519, DOI 10.1002/cpa.3160320403, URL http://dx.doi.org/10.1002/cpa.3160320403
[64] Natterer F (1980) Efficient implementation of 'optimal' algorithms in computerized tomography. Math Methods in the Appl Sciences 2:545–555
[65] Natterer F (2001) The mathematics of computerized tomography. Classics in Mathematics, Society for Industrial and Applied Mathematics, New York
[66] Natterer F, Wübbeling F (2001) Mathematical Methods in image Reconstruction. Monographs on Mathematical Modeling and Computation, Society for Industrial and Applied Mathematics, New York
[67] Nolan CJ (2000) Scattering in the presence of fold caustics. SIAM J Appl Math 61(2):659–672, DOI 10.1137/S0036139999356107, URL http://dx.doi.org/10.1137/S0036139999356107
[68] Nolan CJ, Cheney M (2004) Microlocal analysis of synthetic aperture radar imaging. J Fourier Anal Appl 10(2):133–148, DOI 10.1007/s00041-004-8008-0, URL http://dx.doi.org/10.1007/s00041-004-8008-0
[69] Öktem O (2014) The mathematics of eletron microscopy. In: Scherzer O (ed) The Handbook of Mathematical Methods in Imaging, 2nd edn, Springer Verlag, New York
[70] Park JM, Jr EAF, Garg M, Fajardo LL, Niklason LT (2007) Breast Tomosynthesis: Present Considerations and Future Applications. RadioGraphics 27:S231–S240
[71] Perry RM (1977) On reconstructing a function on the exterior of a disc from its Radon transform. J Math Anal Appl 59:324–341
[72] Petersen B (1983) Introduction to the Fourier Transform and Pseudo-Differential Operators. Pittman, Boston
[73] Quinto ET (1983) Singular value decompositions and inversion methods for the exterior Radon transform and a spherical transform. J Math Anal Appl 95:437–448

[74] Quinto ET (1988) Tomographic reconstructions from incomplete data–numerical inversion of the exterior Radon transform. Inverse Problems 4:867–876
[75] Quinto ET (2006) Support Theorems for the Spherical Radon Transform on Manifolds. International Mathematics Research Notices 2006:1–17, article ID = 67205
[76] Quinto ET (2007) Local Algorithms in Exterior Tomography. Journal of Computational and Applied Mathematics 199:141–148
[77] Quinto ET, Öktem O (2008) Local tomography in electron microscopy. SIAM J Appl Math 68:1282–1303
[78] Quinto ET, Rullgård H (2013) Local singularity reconstruction from integrals over curves in R^3. Inverse Problems and Imaging 7(2):585–609
[79] Quinto ET, Bakhos T, Chung S (2008) A local algorithm for Slant Hole SPECT. In: Mathematical Methods in Biomedical Imaging and Intensity-Modulated Radiation Therapy (IMRT), Centro De Georgi, Pisa, Italy, pp 321–348, cRM Series, Volume 7
[80] Quinto ET, Skoglund U, Öktem O (2009) Electron lambda-tomography. Proc Nat Acad Sci USA 106(51):21,842–21,847
[81] Radon J (1994) Über die Bestimmung von Funktionen durch ihre Integralwerte längs gewisser Mannigfaltigkeiten. In: 75 years of Radon transform (Vienna, 1992), Conf. Proc. Lecture Notes Math. Phys., IV, Int. Press, Cambridge, MA, pp 324–339
[82] Ramachandran G, Lakshminarayanan A (1971) Three dimensional reconstruction from radiographs and electron micrographs: applications of convolutions instead of Fourier Transforms. Proc Natl Acad Sci USA 68:262–277
[83] Rudin W (1973) Functional analysis. McGraw-Hill Book Co., New York, mcGraw-Hill Series in Higher Mathematics
[84] Shepp LA, Kruskal JB (1978) Computerized Tomography: The new medical X-ray technology. Amer Mathematical Monthly 85:420–439
[85] Shepp LA, Srivastava S (1986) Computed tomography of PKM and AKM exit cones. A T & T Technical J 65:78–88
[86] Shubin MA (2001) Pseudodifferential operators and spectral theory, 2nd edn. Springer-Verlag, Berlin, translated from the 1978 Russian original by Stig I. Andersson
[87] Smith KT, Solmon DC, Wagner SL (1977) Practical and mathematical aspects of the problem of reconstructing objects from radiographs. Bull Amer Math Soc 83:1227–1270
[88] Stefanov P, Uhlmann G (2013) Is a curved flight path in SAR better than a straight one? SIAM J Appl Math 73(4):1596–1612
[89] Strichartz RS (1982) Radon Inversion–Variations on a Theme. American Mathematical Monthly 89:377–384
[90] Taylor ME (1981) Pseudodifferential operators, Princeton Mathematical Series, vol 34. Princeton University Press, Princeton, N.J.

[91] Trèves F (1980) Introduction to pseudodifferential and Fourier integral operators. Vol. 1. Plenum Press, New York, pseudodifferential operators, The University Series in Mathematics
[92] Trèves F (1980) Introduction to pseudodifferential and Fourier integral operators. Vol. 2. Plenum Press, New York, fourier integral operators, The University Series in Mathematics
[93] Vainberg E, Kazak IA, Kurozaev VP (1981) Reconstruction of the internal three-dimensional structure of objects based on real-time integral projections. Soviet Journal of Nondestructive Testing 17:415–423
[94] Vaughan CL (2008) Imagining The Elephant: A Biography of Allan Macleod Cormack. Imperial College Press, London, UK
[95] Yarman CE, Yazıcı B, Cheney M (2008) Bistatic synthetic aperture radar imaging for arbitrary flight trajectories. IEEE Trans Image Process 17(1):84–93
[96] Yazici B, Cheney M, Yarman C (2006) Synthetic-aperture inversion in the presence of noise and clutter. Inverse Problems 22:1705–1729
[97] Ye Y, Yu H, Wang G (2007) Cone beam pseudo-lambda tomography. Inverse Problems 23:203–215
[98] Ye Y, Yu H, Wang G (2008) Exact interior reconstruction from truncated limited-angle projection data. International Journal of Biomedical Imaging 6
[99] Yu H, Wang G (2009) Compressed sensing based interior tomography. Physics in Medicine and Biology 54:2791–2805
[100] Zalcman L (1980) Offbeat Integral Geometry. Amer Math Monthly 87:161–175
[101] Zalcman L (1982) Uniqueness and nonuniqueness for the Radon transform. Bull London Math Soc 14(3):241–245, DOI 10.1112/blms/14.3.241
[102] Zampighi G, Zampighi L, Fain N, Wright E, Cantelle F, Lanzavecchia S (2005) Conical tomography II: A method for the study of cellular organelles in thin sections. Journal of Structural Biology 151(3):263–274